PROCEEDINGS A

royalsocietypublishing.org/journal/rspa

Research

Cite this article: Cattell O, Mayora-Cebollero A, O'Dea RD, Barrio R, Coombes S. 2026 Understanding tonic–clonic seizure transitions as secondary bifurcations in a neural field model. *Proc. R. Soc. A* **482**: 20250452. https://doi.org/10.1098/rspa.2025.0452

Received: 23 May 2025
Accepted: 5 March 2026

Subject Areas:
applied mathematics

Keywords:
neural field, epilepsy, seizure, torus bifurcation, Turing Instability, quasi-periodic transition

Author for correspondence:
S. Coombes
e-mail: stephen.coombes@nottingham.ac.uk

Electronic supplementary material is available online at https://doi.org/10.6084/m9.figshare.c.8459650.

THE ROYAL SOCIETY PUBLISHING

Understanding tonic–clonic seizure transitions as secondary bifurcations in a neural field model

O. Cattell[1], A. Mayora-Cebollero[2], R. D. O'Dea[1], R. Barrio[2] and S. Coombes[1]

[1]School of Mathematical Sciences, University of Nottingham, Nottingham NG7 2RD, UK
[2]Department of Applied Mathematics and IUMA, Universidad de Zaragoza, Zaragoza 50009, Spain

AMC, 0000-0002-4802-2511; RDO'D, 0000-0002-1284-9103; RB, 0000-0002-8089-343X; SC, 0000-0003-1610-7665

Epilepsy is a dynamic complex disease involving a paroxysmal change in the activity of millions of neurons, often resulting in seizures. Tonic–clonic seizures are a particularly important class of these and have previously been theorized to arise in systems with an instability from one temporal rhythm to another via a quasi-periodic transition. We show that a recently introduced class of *next-generation* neural field models has a sufficiently rich bifurcation structure to support such behaviour. A linear stability analysis of the space-clamped model is used to uncover the conditions for a Hopf–Hopf bifurcation whereby two incommensurate frequencies can be excited. This is used to seed a more exhaustive numerical bifurcation analysis that highlights the preponderance of the model to generate torus bifurcations. Since the neural field model is derived from a biophysically meaningful spiking tissue model, we are able to highlight the neurobiological mechanisms that can underpin tonic–clonic seizures as they relate to levels of excitability, electrical and chemical synaptic coupling and the speed of action potential propagation. We further show how spatio-temporal patterns of activity can evolve in the fully nonlinear regime using direct numerical simulations far from a Turing bifurcation.

1. Introduction

Epilepsy is a common neurological condition affecting over 50 million people globally [1]. It is characterized by recurrent, unprovoked seizures that signify a paroxysmal change in neurological functions associated with hyper-synchronization of neurons [2]. Epileptic seizures show huge variation in their presentation and a classification model has been developed to aid clinicians in diagnosis and management [3]. The importance to study seizure dynamics not as a generic event but rather specific to different classes of seizure is clear. An important class of seizure is that of *tonic–clonic* type (historically, 'grand mal'). These seizures contain two key phases. In the tonic phase, a high-frequency electro-encephalography (EEG) oscillation occurs, resulting in a loss of consciousness and muscular stiffness. This high-frequency oscillation then transitions via an aperiodic transient phase into the clonic phase in which a new frequency dominates and gives rise to rhythmic muscular jerks. In 1980, Ermentrout & Cowan suggested that the evolution of an ictal seizure through tonic and clonic stages could be described by a secondary bifurcation in a dynamical system that linked one branch of periodic orbits with another [4]. This was argued for on general grounds using ideas from symmetric bifurcation theory in the context of a Wilson–Cowan neural field model. This is a simple phenomenological model of neural tissue that can be written as an integro-differential equation with a sigmoidal nonlinearity to capture the notion of tissue firing rate; see [5] for a recent perspective. The work in [4] did not provide a methodology for computing or classifying seizure-like transitions in neural fields and subsequent work has suggested that it is challenging to find open parameter sets that support tonic–clonic transitions in standard neural fields [6]. Thus, it is interesting to look for more principled neural field models that can more readily exhibit such epileptic transitions. It is natural to consider the incorporation of more biophysically realistic model components than in standard neural field models, say including models of chemical synapses that include shunting terms (mediated by synaptic reversal potentials) as well as electrical ones that are known to be important in epilepsy [7]. The latter are often not included in standard neural field models because their link to microscopic dynamics (single cell voltage) is often hard to reconcile with the coarse-grained variables of standard phenomenological neural field models. Of course, one could also consider the study of spiking, as opposed to rate-based, neural fields as in [8], although this leads to substantial mathematical and computational challenges as compared to their rate-based counterparts.

In this paper, we consider a recently developed class of so-called *next-generation* neural field models demonstrating that they exhibit a sufficiently rich bifurcation structure to support the type of transitions hypothesized by Ermentrout & Cowan to describe tonic–clonic seizures. This mean-field model can be derived from an underlying system of spiking θ-neurons, with the inclusion of both chemical and electrical synapses, yet is of itself a rate-based neural field model. It differs from more traditional Wilson–Cowan-like neural fields in the sense that the firing rate is a *derived* quantity and dynamically tracks the level of coherence (synchrony) within a localized region of tissue. Moreover, the formal equivalence of the θ-neuron to a voltage based quadratic integrate-and-fire (QIF) neuron gives a corresponding mean-field description in terms of a coupled dynamical system for the simultaneous evolution of mean membrane potential and population firing rate. Thus, the field model can naturally describe the evolution of patterns of synchrony, allowing a direct interpretation in terms of seizure states associated with hyper-synchronization, as well track the more traditional notion of population firing rate that has been the mainstay of neural field modelling for many years. The major theoretical breakthroughs that have engendered this are based on exact solutions for the density of states in large θ-neuron networks developed by Luke *et al*. [9] (exploiting the Ott–Antonsen ansatz) and Montbrió *et al*. [10] (exploiting the Lorentzian ansatz) for QIF networks. For recent expositions on the use of these approaches in neural activity modelling, see [11,12]. These next-generation models, and their variations, have been used in a wide range of applications, including: understanding post movement β-rebound [13], as generative models for EEG and magneto-encephalography [14] and modelling whole-brain resting state dynamics [15]. More recently, the inclusion of electrical

synapses within the modelling framework has shown that the strength of gap junction coupling is a key parameter for enhanced model fitting to empirical whole-brain functional connectivity data [16].

In §2, we introduce the next-generation neural field model of cortical activity that we consider throughout the remainder of the paper. This is cast as a non-local and nonlinear model with space-dependent delays. The latter represents the signalling delays arising from the propagation of action potentials along white-matter tracts and are important for generating realistic spatio-temporal patterns of cortical activity [17]. For ease of direct numerical simulation, we also present an equivalent partial differential equation (PDE) model that can be formulated when synaptic interactions decay exponentially with distance. We begin the mathematical analysis of the model with a linear Turing analysis of the homogeneous steady state in §3. We use this to determine when spatio-temporal travelling wave patterns with incommensurate temporal frequencies can be simultaneously excited. This provides an initial set of parameters around which a systematic study for paths that can link one branch of periodic orbits with another in the fully nonlinear system can be conducted. In §4, we develop this approach for spatially homogeneous solutions. A systematic numerical bifurcation analysis of the *space-clamped* system uncovers a rich fixed point structure in the space of gap junction coupling strengths. On top of this, we build the locus of primary saddle–node, Hopf and Hopf–Hopf bifurcations as well as nearby secondary torus bifurcations. Instances of stable 2-tori solutions are found and their occupation of parameter space is ascertained using a spike-counting technique that can distinguish amongst qualitatively different space-clamped solutions. The calculation of Lyapunov exponents (LEs) is used to characterize windows of chaotic behaviour. From this study, we are able to determine paths in parameter space that can take one through a tonic–clonic seizure state in the space-clamped model and illustrate this with numerical studies and the plotting of spectrograms that show a clear transition from one dominant frequency to another. We define the tonic and clonic oscillations to be the two oscillatory states with fast and slow frequencies, respectively. In §5, we use direct numerical simulations of the full space–time model to uncover the types of nonlinear waves and oscillations that can emerge along tonic–clonic seizure paths. Finally, in §6, we present the conclusions of our work and discuss natural next steps.

2. Neural field model

Assuming that the seizure states commonly recorded in EEG are predominantly a cortical phenomenon it is natural to consider modelling them with a neural field approach. This provides a tissue level continuum description of neural activity, typically posed on a line, plane, sphere or folded surface with dynamics determined by an appropriate integro-differential equation; see [18] for an overview. Non-local spatial interactions arising from long-range axonal fibre tracts are modelled via integral terms, while the intrinsic dynamic of the tissue is modelled with a local set of differential equations. The Wilson–Cowan model is perhaps the most famous exemplar of this type [19,20] and has previously been considered as a candidate model for describing tonic–clonic seizures [4]. However, the simplicity of this phenomenological model appears to preclude it from generating behaviours that can easily switch from one frequency to another via a quasi-periodic transition [6]. Here, we work with a new type of neural field model with a closer relationship to neurobiology in the sense that mean-field neural activity is derived from an underlying population of spiking cells. This model has a much richer bifurcation structure than many previous neural field models of Wilson–Cowan type and importantly, as we shall demonstrate in this paper, the ability to generate a plethora of torus bifurcations that can organize frequency switching. Given that the model includes realistic components for chemical synapses (with reversal potentials and dynamics of conductance changes), electrical synapses (with gap junction coupling) and space-dependent delayed interactions (incorporating the speed of an action potential), it is ideally suited for uncovering potential neurobiological mechanisms of tonic–clonic seizure states. Here, we first describe the mathematical formulation of the mean-field model that consists of interacting excitatory and inhibitory sub-populations, with both reciprocal

and self-connections, embedded in a spatial continuum. For ease of description, we shall pose the model on the real line, though it is easily recast on other spaces. For a recent discussion of the derivation of the mean-field model from a network of QIF neurons, see [14].

To formulate the governing equations for the full neural field model, it is convenient to introduce the labels E and I to distinguish between local excitatory and inhibitory neuronal sub-populations, respectively. The synaptic current induced by a chemical synapse mediating a connection from population b to population a, with $a, b \in \{E, I\}$, is given by a term of the form $g_{ab}(v_{\text{syn}}^{ab} - V_a)$. Here, g_{ab} is a dynamic conductance, v_{syn}^{ab} the synaptic reversal potential and V_a the average (non-dimensionalized) membrane potential in population a. The synapse is said to be excitatory (inhibitory) if the reversal potential is positive (negative) with respect to the steady-state resting potential. The conductance changes induced by activity from population b in population a are denoted by ψ_{ab} and are delayed by the amount of time it takes to propagate an action potential along a connecting axonal fibre. To replicate the rise and fall time of a typical post-synaptic response, described by a normalized α-function of the form $\eta_{ab}(t) = \alpha_{ab}^2 t e^{-\alpha_{ab} t}$ for $t \geq 0$ (with time-to-peak α_{ab}^{-1}), we introduce the temporal differential operator $Q_{ab} = (1 + \alpha_{ab}^{-1}\partial/\partial t)^2$ and write

$$Q_{ab}\, g_{ab}(x,t) = \kappa_s^{ab} \psi_{ab}(x,t) \tag{2.1}$$

and

$$\psi_{ab}(x,t) = \int_{\mathbb{R}} w_{ab}(|x-y|) R_b\left(y, t - \frac{|x-y|}{v_{ab}}\right) \mathrm{d}y, \quad x \in \mathbb{R}. \tag{2.2}$$

Here, κ_s^{ab} is the strength of chemical synaptic coupling, $w_{ab}(x)$ describes the shape of distance dependent coupling and v_{ab} is the speed of an action potential. The inclusion of white-matter delays are important for capturing the spatial distribution of seizure dynamics [21]. The variable $R_b(x,t)$ is the firing rate of population b at position x at time t. The synaptic current induced by an electrical synapse between populations a and b takes the ohmic form $\kappa_v^{ab}(V_b - V_a)$ with κ_v^{ab} denoting the strength of gap junction coupling. The system of equations (2.1)–(2.2) is closed with the prescription for $R_a = R_a(x,t)$, which in turn depends upon $V_a = V_a(x,t)$, each of which are driven by chemical and electrical synapses as

$$\tau_a \frac{\partial R_a}{\partial t} = -R_a \sum_b (g_{ab} + \kappa_v^{ab}) + 2R_a V_a + \frac{\Delta_a}{\pi \tau_a} \tag{2.3}$$

and

$$\tau_a \frac{\partial V_a}{\partial t} = \eta_0^a + V_a^2 - \pi^2 \tau_a^2 R_a^2 + \sum_b g_{ab}(v_{syn}^{ab} - V_a) + \sum_b \kappa_v^{ab}(V_b - V_a). \tag{2.4}$$

Here, τ_a is a membrane time constant, η_0^a a constant background drive and Δ_a a parameter that sets the level of heterogeneity in the underlying spiking QIF model (where each spiking cell has a random background drive drawn from a Lorentzian distribution with centre η_0^a and width at half-maximum Δ_a). From the pair $(V_a(x,t), R_a(x,t))$, the Kuramoto order parameter $Z_a(x,t) \in \mathbb{C}$ describing the level of within-tissue synchrony in population a at position x can be constructed as

$$Z_a = \frac{1 - W_a^*}{1 + W_a^*} \quad \text{and} \quad W_a = \pi \tau_a R_a + i V_a, \tag{2.5}$$

where * denotes the complex conjugate. The full next-generation neural field model is given by equations (2.1)–(2.4) upon specification of the connectivity function w_{ab} which we shall choose to be of the normalized form,

$$w_{ab}(x) = \frac{1}{2\sigma_{ab}} e^{-|x|/\sigma_{ab}}, \tag{2.6}$$

where σ_{ab} is a spatial scale. As well as being a natural choice for describing the spatial decay of interactions in human cortex [22], this particular choice also allows the non-local form of equation (2.2) to be recast as the solution to a PDE often referred to as the *brain wave* equation [23]. This is useful for performing numerical simulations, although numerical approximation of the delayed and non-local term can also be performed for connectivity choices that do not

admit a corresponding PDE description, as in [6]. In appendix A, we provide the forms of the brain wave equation that are used in later direct numerical simulations in both one and two spatial dimensions. For large-scale brain modelling (on the cm scale), it is natural to consider a situation of long-range excitation and short-range inhibition with $\sigma_{aE} > \sigma_{aI}$. A parameter set for this situation is given in Appendix B and denoted P1. Here, parameters for synaptic and membrane time scales, synaptic reversal potentials and the speed of the action potential are set in physiological regimes, whilst other model parameters $(\eta_a, \Delta_a, \kappa_s^{ab})$ are primarily chosen to give realistic emergent frequencies, with the strengths of gap junction coupling κ_v^{ab} treated as bifurcation parameters.

It is important to stress here that we are explicitly including electrical connections between excitatory (pyramidal) cells, as in previous modelling work by Crodelle *et al*. [24,25]. Although electrical connections among cortical interneurons are well known, e.g. [26–28], those between adult cortical pyramidal cells have only recently been discovered [29,30]. Although rarer than electrical connections between interneurons they can be nearly 25 times stronger. Interestingly and in contrast to gap junction coupled interneurons, action potentials have been found to propagate through such junctions. While the protein mediating the electrical coupling between pyramidal cells and between interneurons is probably different, in this paper, we refer to all types of electrical connections with the term 'gap junction coupled' and use a simple ohmic model for all forms of electrical coupling, albeit with differing values of electrical coupling strength.

3. Turing instability analysis

A Turing instability analysis of the neural field model described in §2 is valuable for determining how spatio-temporal structure emerges from otherwise homogeneous neural activity. Importantly, it can help identify critical parameter regimes for the excitation of physiologically important frequencies and, in our case, help reduce large parameter spaces for further exploration in the nonlinear regime with numerical bifurcation analysis of a space-clamped model and direct simulations of the full neural field. In the analysis that follows, we shall fix $v_{ab} = v$ for all (a, b) for simplicity.

Here, we consider perturbations to the homogeneous state which are spatially periodic. This will allow us to determine not only the temporal patterns of activity that can be excited in the neural field model, but also how these are coordinated in space. For the Turing analysis that follows, it is convenient to rewrite equation (2.1) in the integrated form,

$$g_{ab} = \kappa_s^{ab}\eta_{ab} * K_{ab} \otimes R_b, \tag{3.1}$$

where

$$K_{ab}(x,t) = w_{ab}(|x|)\delta(t - |x|/v), \tag{3.2}$$

$$[K_{ab} \otimes R_b](x,t) \equiv \int_{\mathbb{R}} \mathrm{d}s \int_{\mathbb{R}} \mathrm{d}y K_{ab}(y,s) R_b(x-y, t-s) = \psi_{ab}(x,t) \tag{3.3}$$

and

$$[\eta_{ab} * \psi_{ab}](x,t) \equiv \int_0^\infty \mathrm{d}s \eta_{ab}(s)\psi_{ab}(x, t-s). \tag{3.4}$$

Thus, the full neural field model is more succinctly given by equations (2.3), (2.4) and (3.1). Homogeneous steady-state solutions of the form $(R_a(x,t), V_a(x,t)) = (\overline{R}_a, \overline{V}_a)$ satisfy the four nonlinear algebraic equations,

$$\left.\begin{aligned} 0 &= -\overline{R}_a \sum_b (\overline{g}_{ab} + \kappa_v^{ab}) + 2\overline{R}_a\overline{V}_a + \frac{\Delta_a}{\pi\tau_a} \\ \text{and} \quad 0 &= \eta_0^a + \overline{V}_a^2 - \pi^2\tau_a^2\overline{R}_a^2 + \sum_b \overline{g}_{ab}(v_{syn}^{ab} - \overline{V}_a) + \sum_b \kappa_v^{ab}(\overline{V}_b - \overline{V}_a), \end{aligned}\right\} \tag{3.5}$$

where $\overline{g}_{ab} = \kappa_s^{ab}\overline{R}_b$.

Considering linear perturbations to the steady state of the form

$$(R_a(x,t), V_a(x,t), g_{ab}(x,t)) = (\overline{R}_a, \overline{V}_a, \overline{g}_{ab}) + \mathrm{e}^{\mathrm{i}kx}\mathrm{e}^{\lambda t}(\delta R_a, \delta V_a, \delta g_{ab}) \tag{3.6}$$

yields a dispersion relationship for $\lambda = \lambda(k)$ that can be written in the implicit form $\mathcal{E}(k,\lambda) = \det(M(k,\lambda) - \lambda\Upsilon) = 0$, where $\Upsilon = \mathrm{diag}(\tau_E, \tau_I, \tau_E, \tau_I)$ and

$$M(k,\lambda) = \begin{bmatrix} A(k,\lambda) & B \\ C(k,\lambda) & D \end{bmatrix}, \tag{3.7}$$

with 2×2 blocks given by

$$\left.\begin{aligned} A(k,\lambda) &= \begin{bmatrix} 2\overline{V}_E - \overline{R}_E F_{EE}(k,\lambda) - \sum_b(\overline{g}_{Eb} + \kappa_v^{Eb}) & -\overline{R}_E F_{EI}(k,\lambda) \\ -\overline{R}_I F_{IE}(k,\lambda) & 2\overline{V}_I - \overline{R}_I F_{II}(k,\lambda) - \sum_b(\overline{g}_{Ib} + \kappa_v^{Ib}) \end{bmatrix}, \\ B &= \begin{bmatrix} 2\overline{R}_E & 0 \\ 0 & 2\overline{R}_I \end{bmatrix}, \\ C(k,\lambda) &= \begin{bmatrix} -2\pi^2\tau_E^2\overline{R}_E + F_{EE}(k,\lambda)(v_{syn}^{EE} - \overline{V}_E) & F_{EI}(k,\lambda)(v_{syn}^{EI} - \overline{V}_E) \\ F_{IE}(k,\lambda)(v_{syn}^{IE} - \overline{V}_I) & -2\pi^2\tau_I^2\overline{R}_I + F_{II}(k,\lambda)(v_{syn}^{II} - \overline{V}_I) \end{bmatrix} \\ \text{and} \qquad D &= \begin{bmatrix} 2\overline{V}_E - \sum_b \overline{g}_{Eb} & 0 \\ 0 & 2\overline{V}_I - \sum_b \overline{g}_{Ib} \end{bmatrix}. \end{aligned}\right\} \tag{3.8}$$

Here, $F_{ab}(k,\lambda) = \kappa_s^{ab}\widetilde{\eta}_{ab}(\lambda)\widehat{w}_{ab}(k,\lambda)$, where

$$\widetilde{\eta}_{ab}(\lambda) = \int_0^\infty \eta_{ab}(t)\mathrm{e}^{-\lambda t}\mathrm{d}t = \frac{1}{(1+\lambda/\alpha_{ab})^2} \tag{3.9}$$

and

$$\widehat{w}_{ab}(k,\lambda) = \int_{\mathbb{R}} w_{ab}(|x|)\mathrm{e}^{-\lambda|x|/v}\mathrm{e}^{\mathrm{i}kx}\mathrm{d}x. \tag{3.10}$$

For the choice equation (2.6), we have that

$$\widehat{w}_{ab}(k,\lambda) = \sigma_{ab}^{-1}\frac{\sigma_{ab}^{-1} + \lambda/v}{(\sigma_{ab}^{-1} + \lambda/v)^2 + k^2}. \tag{3.11}$$

In order to generate a quasi-periodic transition state, two pairs of purely imaginary eigenvalues must coexist. The ratio of the corresponding frequencies ω_1, ω_2 must be irrational in order for the desired quasi-periodicity to occur. In practice, this means finding a pair of imaginary eigenvalues, defined by the following two complex equations:

$$0 = \mathcal{E}(k, \mathrm{i}\omega)|_{(\omega,k)=(\omega_{1,2},k_{1,2})}, \tag{3.12}$$

and that the dispersion curves tangentially touch the imaginary axis at both $(\omega,k) = (\omega_1,k_1)$ and $(\omega,k) = (\omega_2,k_2)$. This latter condition is equivalent to demanding

$$0 = \left|\frac{\partial(\mathcal{M},\mathcal{N})}{\partial(\omega,k)}\right|_{(\omega,k)=(\omega_{1,2},k_{1,2})}, \tag{3.13}$$

where $\mathcal{M} = \mathrm{Re}(\mathcal{E})$, $\mathcal{N} = \mathrm{Im}(\mathcal{E})$.

To enforce quasi-periodic solutions (in the linearized system), we set ω_1, ω_2 to be irrationally related. Equation (3.12) provides four real (two complex) constraints, and equation (3.13) provides an additional two real constraints. We may allow k_1, k_2 and four selected model parameters to vary. By combining the six real constraints with equation (3.5), a 10-dimensional nonlinear system can be constructed to solve for the steady state, (k_1,k_2) and the four parameters. In this way, one can ascertain when two periodic travelling waves with incommensurate temporal frequencies, of the form $\exp(\mathrm{i}(\omega_{1,2}t + k_{1,2}x))$, can be simultaneously excited.

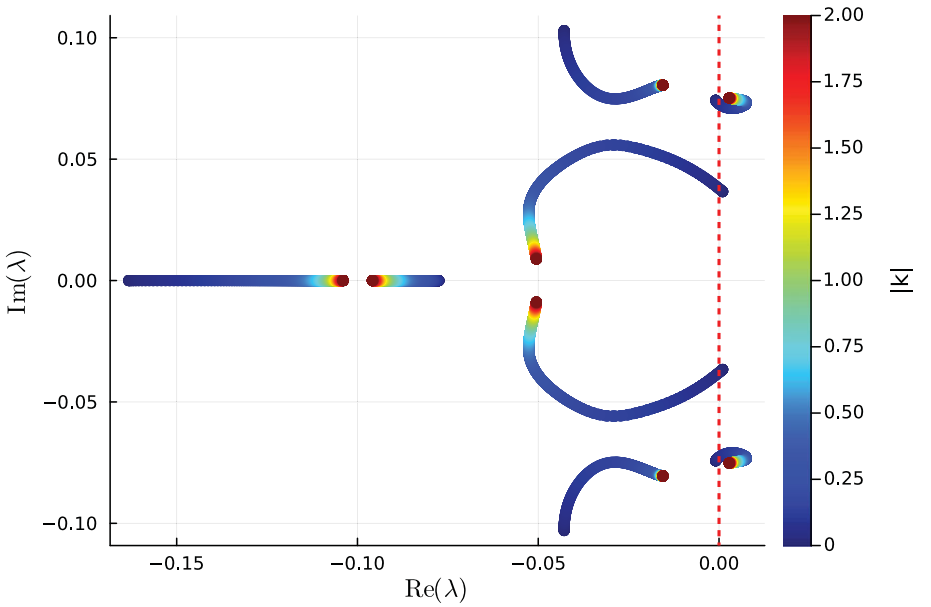

Figure 1. Parameter set P1. Eigenvalue spectrum of the next-generation neural field model after linearizing around the homogeneous steady state with κ_v^{EE}, κ_v^{II} chosen such that there are two branches crossing the imaginary axis at $k = 0$. In this example, the system undergoes an instability arising from a mode with non-zero wavenumber crossing the imaginary axis.

A plot of the eigenvalue spectrum that can be obtained from the Turing analysis is shown in figure 1. Here, the colours attached to each eigenvalue indicate the value of the corresponding wavenumber. In this figure, we have used the parameter set P1 from appendix B with κ_v^{EE}, κ_v^{II} chosen such that there are two branches crossing the imaginary axis at $k = 0$. The crossing at $k = 0$ corresponds to spatially homogenous solutions undergoing a bifurcation. However, the spatially homogenous steady state is already unstable as the spatially inhomogeneous part with $k \neq 0$ in the upper branch has already crossed beyond the imaginary axis giving rise to spatio-temporal patterning.

The analysis performed above is presented in a single spatial dimension. To extend this to two spatial dimensions with spatial perturbations of the form $e^{i\boldsymbol{k}\cdot\boldsymbol{r}}$, $\boldsymbol{k}, \boldsymbol{r} \in \mathbb{R}^2$, we would simply replace the Fourier transform in equation (3.10) by a two-dimensional Fourier transform with spectral parameter $\boldsymbol{k}$ so that $\widehat{w}_{ab}(k, \lambda) \to \widehat{w}_{ab}(|\boldsymbol{k}|, \lambda)$ with

$$\widehat{w}_{ab}(\boldsymbol{k}, \lambda) = \int_{\mathbb{R}^2} w_{ab}(|\boldsymbol{r}|) e^{-\lambda|\boldsymbol{r}|/v} e^{i\boldsymbol{k}\cdot\boldsymbol{r}} d\boldsymbol{r}. \tag{3.14}$$

For the choice

$$w_{ab}(\boldsymbol{r}) = \frac{1}{2\pi\sigma_{ab}^2} e^{-|\boldsymbol{r}|/\sigma_{ab}}, \tag{3.15}$$

we have that

$$\widehat{w}_{ab}(\boldsymbol{k}, \lambda) = \sigma_{ab}^{-2} \frac{\sigma_{ab}^{-1} + \lambda/v}{[(\sigma_{ab}^{-1} + \lambda/v)^2 + \boldsymbol{k}\cdot\boldsymbol{k}]^{3/2}}. \tag{3.16}$$

Finally, note that the linear stability analysis presented above (for steady states) cannot predict the relative amplitudes of each emergent pattern nor their stability. Therefore, to confirm the existence of quasi-periodic solutions in the full spatio-temporal model, we perform numerical simulations at points of interest as suggested by the linear Turing analysis above and the nonlinear space-clamped analysis that follows next and present these in §5.

4. Space-clamped solutions: dynamics and bifurcation analysis

Here, we focus on the analysis of spatially homogenous solutions to the full neural field model. By reducing the spatially extended problem to a lower dimensional system of ordinary differential equations (ODEs), a systematic bifurcation analysis is possible, including studies of primary and secondary bifurcations in one- and two-parameter spaces. In this way, we identify parameter regimes in which instabilities occur, potentially leading to the emergence of spatio-temporal patterns in the full spatial model.

To reduce the model, we seek spatially homogenous solutions to equation (2.4) so that $(g_{ab}(x,t), \psi_{ab}(x,t), R_a(x,t), V_a(x,t)) \to (g_{ab}(t), \psi_{ab}(t), R_a(t), V_a(t))$. These solutions satisfy the full neural field equations (2.1)–(2.4) under the replacement $\partial/\partial t \to \mathrm{d}/\mathrm{d}t$ with

$$\psi_{ab}(t) = \int_{\mathbb{R}} w_{ab}(|y|) R_b(t - |y|/v_{ab}) \mathrm{d}y. \tag{4.1}$$

For the choice equation (2.6), this can be written as the solution to the ODE,

$$\frac{\mathrm{d}\psi_{ab}}{\mathrm{d}t} = \frac{v_{ab}}{\sigma_{ab}}(R_b - \psi_{ab}). \tag{4.2}$$

In this section, we study in detail the parametric structure of the space-clamped next-generation neural field model in the plane of gap junction coupling strengths $(\kappa_v^{EE}, \kappa_v^{II})$. We find it useful to explore two parameter sets, in order to gain insight not only into the mechanisms underlying tonic–clonic seizure transitions in the model, but also into their robustness (in the sense of obviating the need for the fine-tuning of multiple parameters other than those for gap junction strength). We identify tonic and clonic states by their respective frequencies (tonic being faster than clonic) foregoing the use of amplitude information as model components such as $(V_E, R_E, |Z_E|)$ do not correspond directly to clinically observed scalp EEG recordings. The new parameter set P2 is given in appendix B and is not intended to be physiological in the form of its spatial wiring. Rather, we use it to illustrate our numerical methodologies and show that the mechanisms for temporal dynamical transitions in the space-clamped model are relatively robust or insensitive to the choice of wiring. Systematic studies of the more physiological parameter set P1 are also presented, to complement the study in §3 and seed a further numerical study of the full spatial model in §5.

(a) Dynamics for the parameter set P2

First, we consider the parameter set P2. As a preliminary exploration, we show in figure 2 the bifurcation diagrams of some one-parameter lines. If we explore in the $(\kappa_v^{EE}, \kappa_v^{II})$ plane the line $\kappa_v^{II} = 1.8$, we obtain the one-parameter bifurcation diagram of equilibria shown in plot (a1). We plot the parameter κ_v^{EE} on the horizontal axis and the value of the V_E variable on the vertical axis. On the top of plot (a1) (and (b1) and (c1)), we show a horizontal colour bar indicating the number, and stability (U—unstable, S—stable) of the equilibria (and the same colour code is used in figure 3). We have continued the different equilibria and limit cycles using numerical continuation with the MATCONT software [31], and each line in figure 2(a1) represents the V_E variable of each equilibrium point. Note that there are intervals with four and six unstable equilibria and several saddle–node (SN) and Hopf (H) bifurcations appear in the continuation curves. In the plots (a2) and (a3) (as in all the pictures on the right of the figure), we present the continuation of limit cycles generated at some Hopf bifurcations, some of them giving a complete connection between two Hopf bifurcations with a change of direction owing to a saddle–node of limit cycles (plot (a3)) or extending further with increasing κ_v^{EE} as in plot (a2). Also several other bifurcations are present, including Neimark–Sacker (NS) and period-doubling (PD) bifurcations. In plots (b1), (b2), (b3) and (b4), we present some one-parameter bifurcation diagrams in κ_v^{II} for $\kappa_v^{EE} = 2$. And finally, in plot (c1), we explore a situation with $\kappa_v^{II} = 3.5$. All single-parameter studies show several bifurcations and changes that motivate additional two-parameter studies (figures 3, 4, 5, 6 and 7) that will allow us to better understand the overall bifurcation landscape and possible pathways

for different dynamics which is one of the main goals of this article. The one-parameter studies presented here in plots (a1)–(a3) with fixed κ_v^{II} and plots (b1)–(b4) with fixed κ_v^{EE} are *slices* through the two-parameter study shown later in figure 5 (as vertical and horizontal white lines, labelled by V and H, respectively).

In figure 3, we present a plot of the equilibrium structure of the model, showing the number of homogeneous fixed points in the two-parameter $(\kappa_v^{EE}, \kappa_v^{II})$ plane. The colours of each region denote the different number of equilibria and the labels of the form mUnS indicate a region with m unstable and n stable equilibria, respectively. Owing to the high dimension of the system and its complexity there are up to eight equilibria in the studied plane, but at most two stable. Plot (b) presents a magnification around the central part of plot (a) where a more complex structure is detected. Numerous changes in the number of equilibria and in their stability indicate the presence of different bifurcations such as Hopf and saddle–node bifurcations that are studied in detail below.

There are large regions of the studied $(\kappa_v^{EE}, \kappa_v^{II})$ plane where equilibria are unstable. In these situations, the dynamics is expected to be attracted to another kind of dynamic invariant, such as a periodic orbit, an invariant torus or a chaotic attractor. Periodic orbits can naturally be distinguished by the number of *spikes* they show per period, as is commonly done in the classification of bursting orbits seen in single cell neuroscience studies. In figure 4, we use a spike-counting technique [32] to illustrate this; see appendix C for more details. The colour in figure 4 indicates the number of spikes in each cycle of an orbit. A large number of spikes is associated with very long periodic orbits, chaotic behaviour or a torus, and is indicated with dark red colouring. The slightly lighter blue area (second and fourth quadrants) represents spiking behaviour (a periodic orbit with just one loop or peak). The third quadrant manifests a dark blue colour indicative of one stable equilibrium point (no spikes). In contrast, in the first quadrant, the behaviour is highly complex. There are dense bands of different intermediate colours denoting periodic orbits with more than one loop, and bands of dark red colour that may denote long-period periodic orbits, tori or chaotic attractors. In figure 4b, a magnification around the centre part is presented, and here a large degree of complexity in the spike count is readily observed. This suggests that a plethora of bifurcations of codimension one and two are expected to be present in this region.

In order to begin to understand, classify and organize the dynamics that can emerge in regions such as those delineated in figure 4b, it is useful to use a suite of complementary numerical techniques. In figure 5, we present the calculation of the first LEs using the algorithm in [33]; see appendix C for more details. In plot (a), we present again the spike-counting plot of panel (a) of figure 4 to illustrate the cross sections, shown as horizontal (H) and vertical (V) white lines, that we shall focus upon in more detail. In plot (H1), we present the first two LEs. This shows that there are intervals with positive LEs, indicating chaotic attractors. Plot (H2) shows the spike-count measure indicating the number of spikes per cycle. The maximum number represented is 8, and when the value is 8 it indicates either a periodic orbit with a large number of loops, a torus or a chaotic attractor. For the interval shown, no torus solutions are found. Plot (H3) presents a bifurcation diagram showing windows of both periodic orbits and chaotic attractors. More interesting behaviour is observed on the vertical line. In plot (V1), we present the first four LEs. On the interval shown, the dynamics is very complex. There are intervals with chaotic attractors, but also torus and hyper-chaotic attractors as shown in the magnification (V1b). Plot (V2) shows the spike-count measure and plot (V3) presents a bifurcation diagram. In this case, chaotic attractors are evident, but also a torus or NS bifurcation, as is more clearly seen in the magnified view of plot (V3b).

We have identified a plethora of different dynamics in the model, and so it is natural to ask about their origin. To gain some insight into this, we have generated the locus of bifurcations of both equilibria and limit cycles using numerical continuation with the MATCONT software [31]. In figure 6 we show in plots (a) and (a1) the basic bifurcations of equilibria: saddle–node (SN label) and Hopf (H label) curves and some codimension-two bifurcations in the magnified plot (a1), over the equilibria plots of a greyscale version of figure 3. Here, we clearly observe an expected

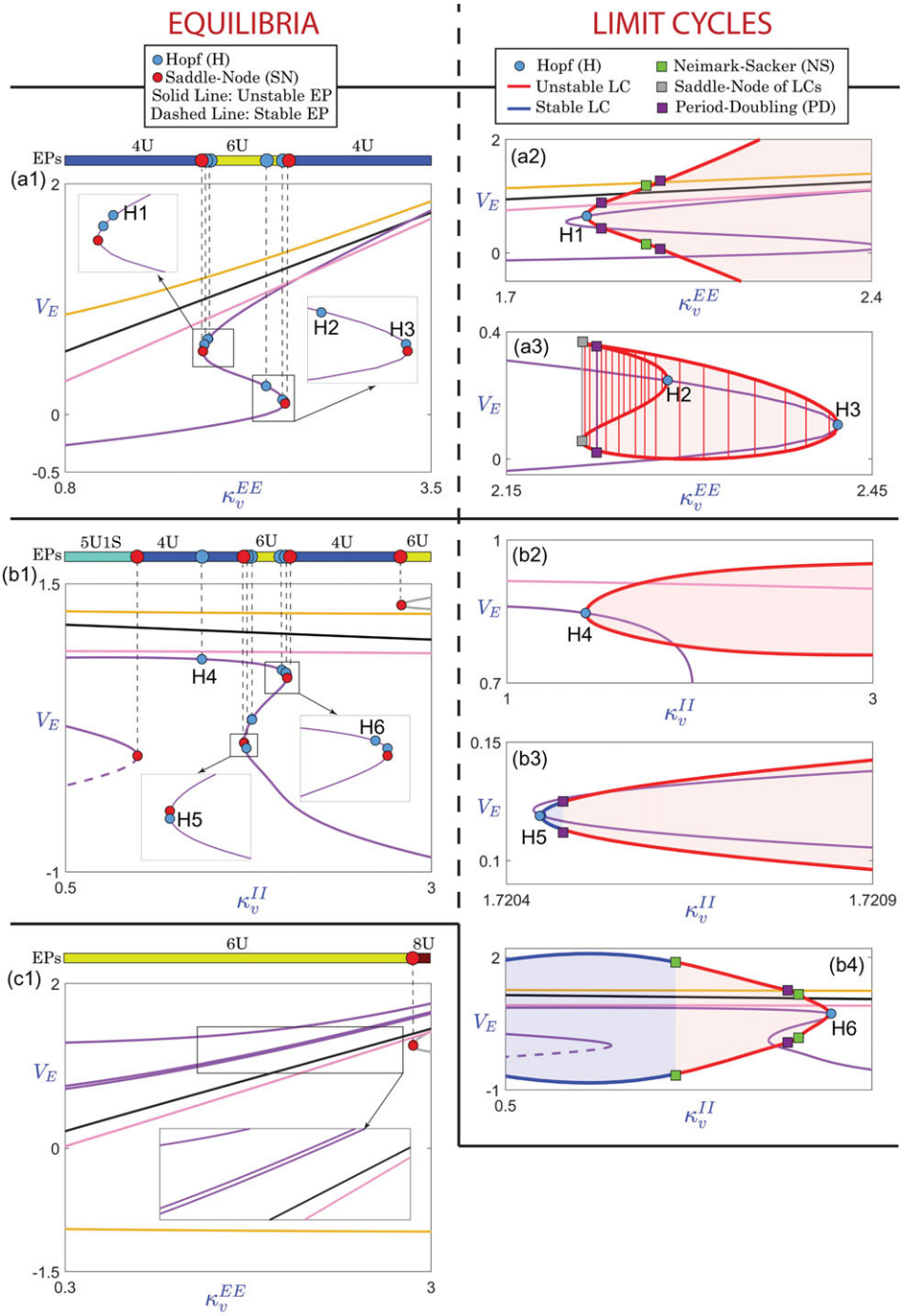

Figure 2. Parameter set P2. (a1) One-parameter bifurcation diagram of equilibria (EPs) for $\kappa_v^{II} = 1.8$. (a2)–(a3) One-parameter bifurcation diagrams of limit cycles (LCs) emerging from H1, H2 and H3. (b1) One-parameter bifurcation diagram of equilibria for $\kappa_v^{EE} = 2$. (b2)–(b3)–(b4) One-parameter bifurcation diagrams of limit cycles emerging from H4, H5 and H6. (c1) One-parameter bifurcation diagram of equilibria for $\kappa_v^{II} = 3.5$. In the bifurcation diagrams of limit cycles, the maximum and minimum of limit cycles have been drawn, and for (a3) the complete range of limit cycles is depicted to clearly show the loop generated by the saddle–node of limit cycles. The horizontal colour bars above the panels (a1)–(b1)–(c1) show the number of equilibria and their stability (U—unstable, S—stable) using the same colour code of figure 3. Note that the lines studied in (a1)–(a2)–(a3) and in (b1)–(b2)–(b3)–(b4) correspond with the ones analysed in figure 5.

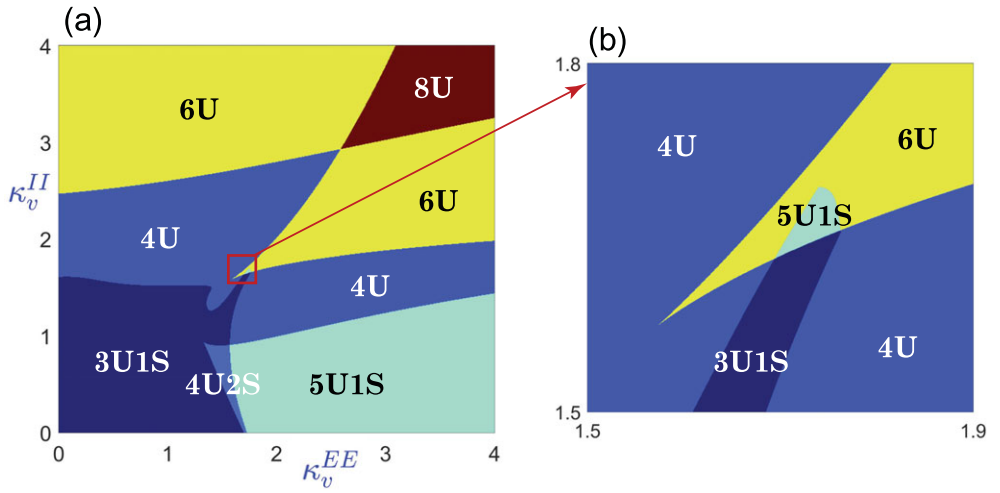

Figure 3. Parameter set P2. Equilibrium structure of the space-clamped next-generation neural field model defined in §4. (a) Plot showing the number of homogeneous fixed points in the parameter plane of gap junction coupling strengths $(\kappa_v^{EE}, \kappa_v^{II})$. The labels *m*U*n*S indicate *m* unstable and *n* stable equilibria. Other parameters in the model are fixed as in appendix B. (b) Magnification around the centre part of plot (a).

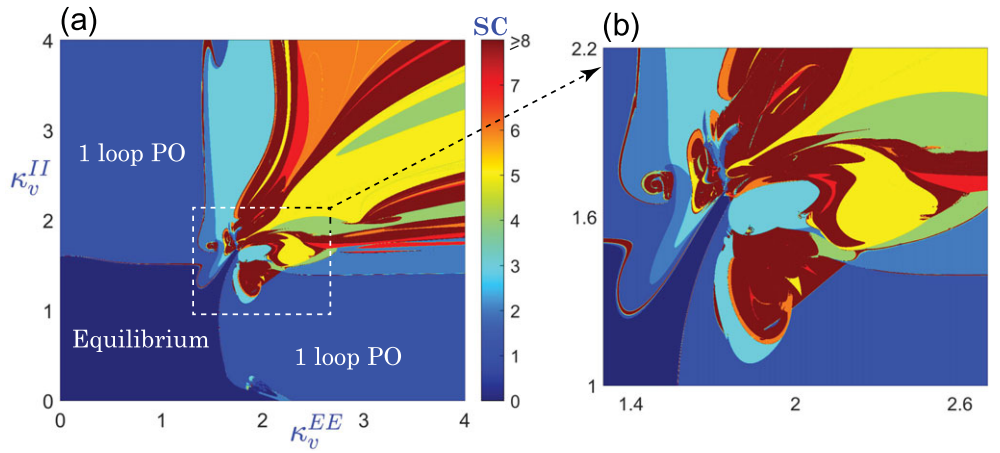

Figure 4. Parameter set P2. A plot of the spike count (SC) for the space-clamped next-generation neural field model in the $(\kappa_v^{EE}, \kappa_v^{II})$ parameter plane for the parameters of figure 3. The region with dark blue colouring has one stable equilibrium point, the lighter blue region supports a periodic orbit (PO) with one loop, and hotter colours indicate an increasing number of spikes associated with chaotic behaviour or a torus.

matching between equilibria borders and bifurcations. In plots (b) and (b1), we detail all the bifurcations of equilibria and limit cycles: the saddle–node (SN label), Hopf (H label) and Hopf–Hopf (HH label) bifurcations of equilibria, as well as secondary torus or NS bifurcations, and some additional codimension-two bifurcation points (zero-Hopf (ZH), Generalized Hopf (GH), Bogdanov–Takens (BT) and cusp point (CP)). We observe that the bifurcation structure is highly complex, especially near one of the codimension two cusp bifurcation points of the augmented region in plot (b1), where many different bifurcations exist, leading to the development of several codimension two bifurcation points. Therefore, there is a sufficient mechanism to create chaotic dynamics as we have already observed in figure 5 (where the first LE is positive in some regions). For our purposes, we consider some NS bifurcation curves that originate at Hopf–Hopf points

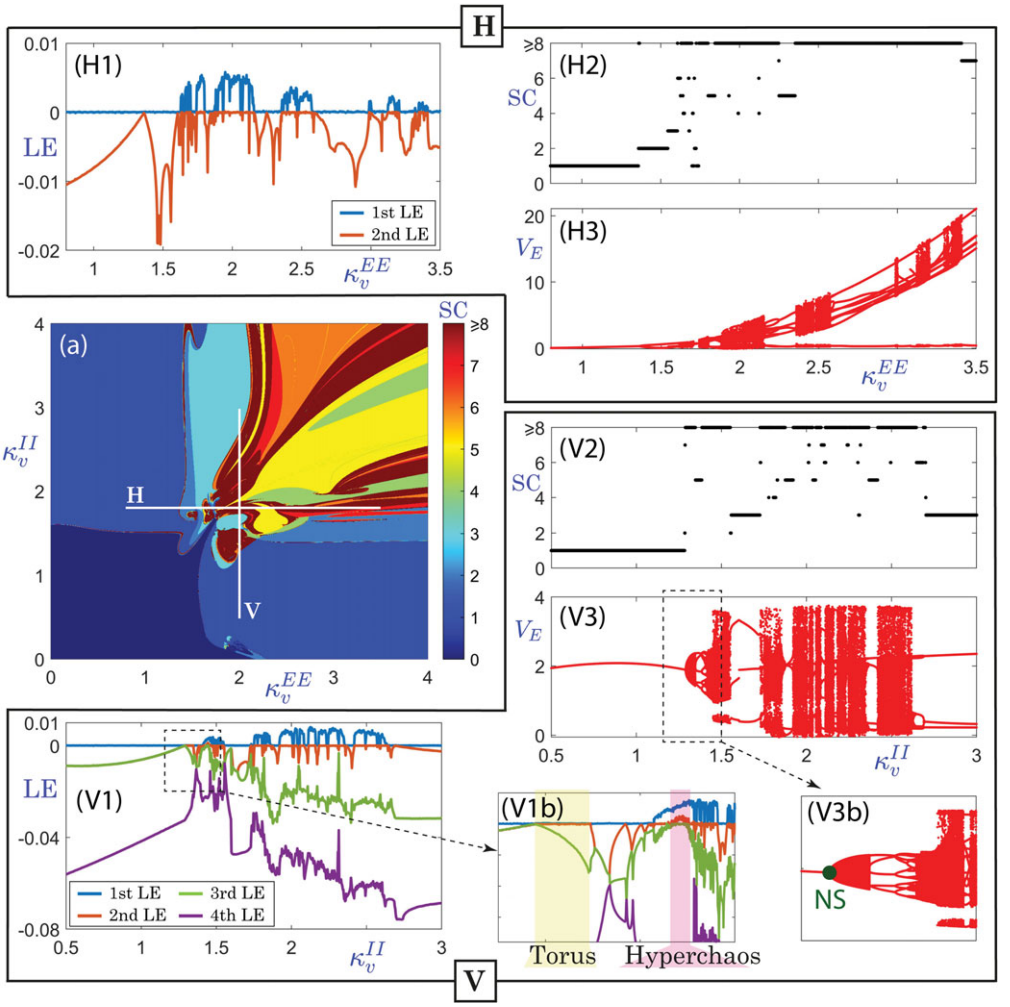

Figure 5. Parameter set P2. (a) Spike-counting (SC) parameter slice through figure 4. (H1), (H2) and (H3) show the first Lyapunov exponents (LEs), the spike-counting values and the bifurcation diagram, respectively, on the horizontal line fixing the parameter κ_v^{II} to 1.8 and the parameter κ_v^{EE} takes values in [0.8, 3.5]. (V1) and (V1b), (V2), and (V3) and (V3b) show the first LEs, the spike-counting values and the bifurcation diagram, respectively, on the vertical line fixing the parameter κ_v^{EE} to 2 and the parameter κ_v^{II} takes values in [0.5, 3.0].

(for a theoretical unfolding of two Hopf–Hopf scenarios see appendix D). On these NS bifurcation curves, 2-torus orbits (two-frequency torus) are generated. One of these curves generates the torus indicated in figure 5(V1b) (and we note that there are also other bifurcation curves). Finally, in plots (c) and (c1) of figure 6, bifurcations are superimposed on a greyscale version of the spike-counting figures of figure 4. Again, the bifurcations define quite well some of the regions detected with the spike-counting method. As in the previous plots, it is important to remark that the existence of several Hopf–Hopf bifurcations lead to the existence of secondary torus or NS bifurcations that give rise to the creation of, among others, a 2-torus orbit as described above. Therefore, figure 6 presents a combination of different techniques, bifurcation analysis, classification of equilibria and spike-counting, that allow us to describe the great complexity of the model, specially at the augmented box of plots (a1), (b1) and (c1), where many different dynamics are observed, from equilibria, periodic orbits, tori and chaotic attractors.

In figure 7, we show different dynamics, from several stable periodic orbits (b)(clonic)–(c)(tonic) to emergent torus solutions (d)–(f), quasiperiodic (or chaotic Feigenbaum) orbits (e) and

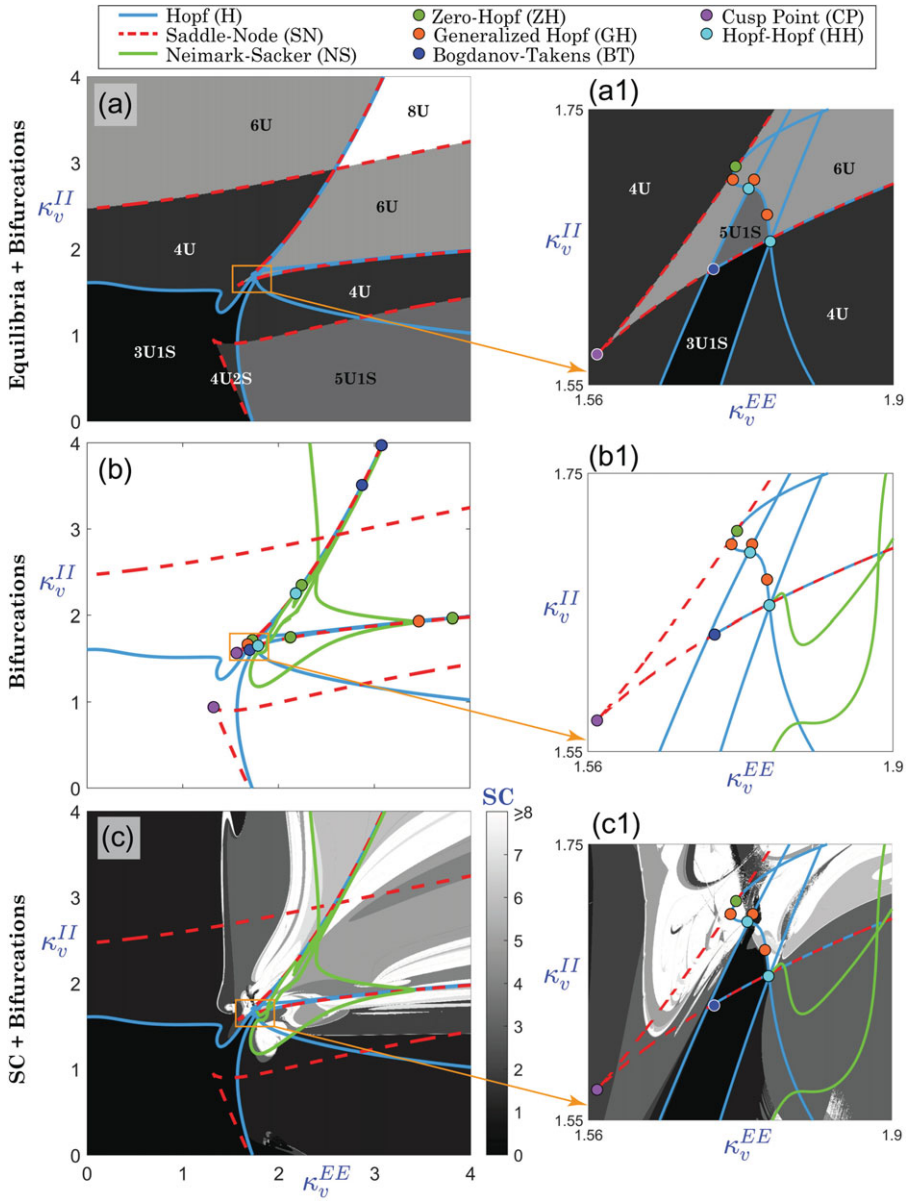

Figure 6. Parameter set P2. (a) and (a1) Primary bifurcations of equilibria superimposed over a greyscale version of figure 3. (b) and (b1) Primary bifurcations of equilibria and limit cycles and several codimension-two points, as well as secondary torus or NS bifurcations. In plots (c) and (c1), the bifurcations are superimposed on a greyscale version of figure 4.

chaotic dynamics (g). In the plots (b)–(g), we show a three-dimensional plot of the orbit in the (V_E, R_E, V_I) variables to illustrate the different kind of dynamics and the time series of $|Z_E|$ and V_E variables. All of these orbits can be connected by small changes in the parameter space (in the plot most of the orbits are connected through a circular parametric route), which means that several changes in the conditions of the system may allow the transitions among all these different dynamics (the positions of the orbits in the two-parameter plane are shown in panel (a)). The equations of the circular parametric path we have followed are given by $\kappa_v^{EE} = 1.7 + 0.7\cos(\gamma - 3\pi/4)$, $\kappa_v^{II} = 1.65 + 0.5\sin(\gamma - 3\pi/4)$, $\gamma \in [0, 7\pi/4]$. The values for the parameters $(\kappa_v^{EE}, \kappa_v^{II})$ used to obtain the orbits of panels (b)–(g) are $(1, 1.6500)$, $(1.5917, 1.1560)$, $(1.7911, 1.6396)$, $(1.9166, 1.1745)$, $(2, 1.3250)$ and $(1.9248, 2.1235)$, respectively. The initial conditions are set to 0 in all orbits, except

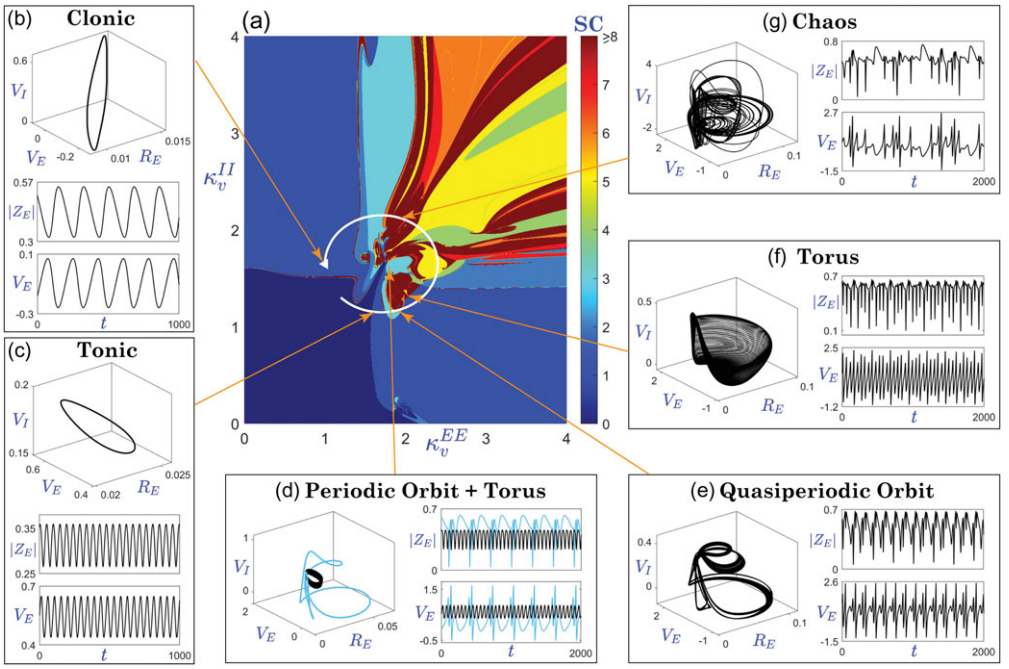

Figure 7. Parameter set P2. Plots of emergent torus solutions at points across the parameter space of figure 6. (a) Two-parameter spike-counting (SC) plot of figure 4 with a circular path from tonic to clonic patterns. (b) and (c) Periodic orbits (fast tonic and slow clonic dynamics). (d) Coexistence of a torus and a periodic orbit. (e) and (f) Tori or quasiperiodic dynamics. (g) Chaotic attractor.

for panel (d), where $(g_{EE}, h_{EE}, g_{II}, h_{II}, g_{EI}, h_{EI}, g_{IE}, h_{IE}, \psi_{EE}, \psi_{II}, \psi_{EI}, \psi_{IE}, R_E, V_E, R_I, V_I) = (0.0734, 0.0631, 0.0343, 0.0334, 0.0687, 0.0668, 0.0419, 0.0361, 0.0159, 0.0161, 0.0161, 0.0159, 0.0161, 0.5908, 0.0168, 0.5346)$ is chosen to reach the torus instead of the coexisting periodic orbit. Note that, in panel (d), we show how periodic orbits and stable tori coexist, giving rise to a highly complex multistability in the model.

Figure 6 suggests that the necessary dynamics for the tonic–clonic seizure transition can be found organized around the central Hopf–Hopf bifurcation. To recreate plausible dynamics in time, we can envisage a slow variation of parameters that takes one on a path through parameter space in which the system starts in the non-oscillatory state modelling the non-seizure state and then orbits through parameter space around the central Hopf–Hopf bifurcation. The system will first transition into the seizure via a Hopf bifurcation giving rise to oscillations at a single frequency. As the system then moves into the transition region, the single frequency gives way to more complex behaviour and quasi-periodicity. As the system approaches the bifurcation boundary the new frequency becomes dominant until a simple limit cycle is restored on crossing the bifurcation boundary. The seizure may then progress back beyond the Hopf bifurcation corresponding to the seizure termination or may remain in this final state. Figure 8 demonstrates an example trajectory in which the model parameters slowly vary along an arc in the $(\kappa_v^{EE}, \kappa_v^{II})$ plane traversing around the organizing region identified by the numerical bifurcation analysis.

To motivate this path, we hypothesize the following mechanism. At the initiation of the seizure, extracellular potassium increases while calcium decreases [34]. Reduced extracellular calcium has been shown to open connexin hemichannels (forming half of a gap junction) in the cell membrane [35] and may show the same effect in full gap junctions. The gap junctions close at large extracellular potassium concentrations owing to the concurrent acidification of the extracellular space [36] resulting in a decrease in effective gap junction coupling. Finally, owing to the large imbalance in numbers of gap junctions between inhibitory and excitatory neurons, the relative

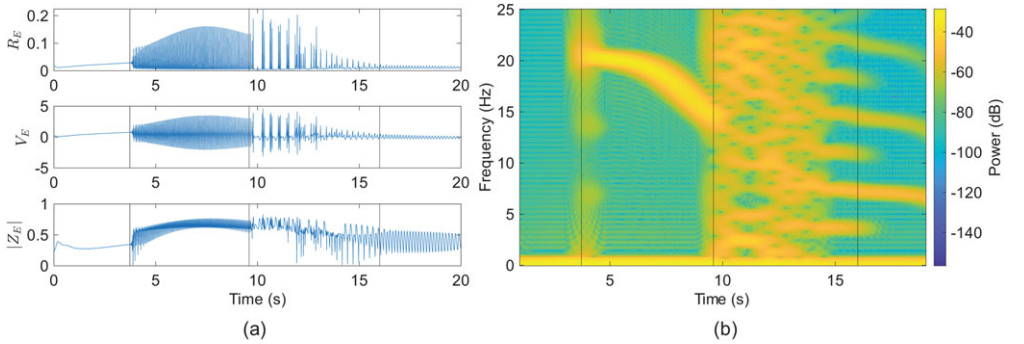

Figure 8. Parameter set P2. Dynamics of the space-clamped model following a slowly varying path travelling anticlockwise through parameter space as shown as a white curve in figure 7. The path passes around the complex region of bifurcation points containing the Hopf–Hopf bifurcation. (a) Time series in R_E, V_E, and $|Z_E|$ of the space-clamped model. The initial steady state goes unstable through a Hopf bifurcation, the resultant limit cycle then loses stability and the system passes through the transition region before finally leading back to a pure limit cycle. Black lines indicate crossings of the Hopf bifurcation lines. (b) The corresponding spectrogram generated using a short-time Fourier transform of the generated time series for R_E in the space-clamped model, with black lines to indicate crossing of bifurcations.

increases and decreases in gap junction coupling may not simultaneously lead to the proposed path.

To clearly see the underlying dynamics in the time series, we produce a spectrogram, shown in figure 8b, with a short-time Fourier transform of the R_E time series. The signal is first resampled to a uniform sampling rate of 1000 Hz and then segmented into windows of 100 ms with a 99 ms overlap. The spectrum for each window is computed with a fast Fourier transform. The spectrogram shows the onset of a clear single-frequency oscillation following the initial Hopf bifurcation, as the system approaches the NS bifurcation the frequency decreases. At bifurcation, the single-frequency state becomes unstable and is replaced by complex dynamics with a complex spectrum across the frequency range. This structure is a result of the relatively short time and the high density of different dynamics in this region as shown in figure 4. When tracing through the parameter space, there is not enough time for the system to track each state faithfully as it crosses through periodic orbits, tori and chaotic regions resulting in a broad complex spectrum for most of this region. As the system approaches the second NS bifurcation, a toroidal solution appears with two frequencies. Finally, one frequency goes unstable leaving a periodic orbit at a single frequency.

(b) Dynamics for the parameter set P1

We now return to the parameter set P1 initially used in figure 1 that is relevant to large-scale brain studies with long-range excitation and short-range inhibition. We shall see below that the narrative for tonic–clonic seizure mechanisms developed above, in terms of paths through the $(\kappa_v^{EE}, \kappa_v^{II})$ plane, is essentially unchanged. This highlights the robustness of the mechanism and that fine-tuning of parameters within a next-generation neural field model is not needed, at least when considering space-clamped solutions.

In figure 9, we present in plot (a) the spike-counting diagram in the $(\kappa_v^{EE}, \kappa_v^{II})$ plane. Similar to figure 4, we observe a rich structure (yet different). In figure 9b a magnification around the central part is presented, and here we also present results for different sets of initial conditions to highlight the possibility of multistability. In the plots 1–4, the plot (b) is repeated but now fixing as initial conditions the last point of the simulation of the previous parameter set moving in four different directions, from bottom to top (–1–), and so on, as explained in picture (b). Note that the pictures have differences in some of the regions indicating multistability among different kind of

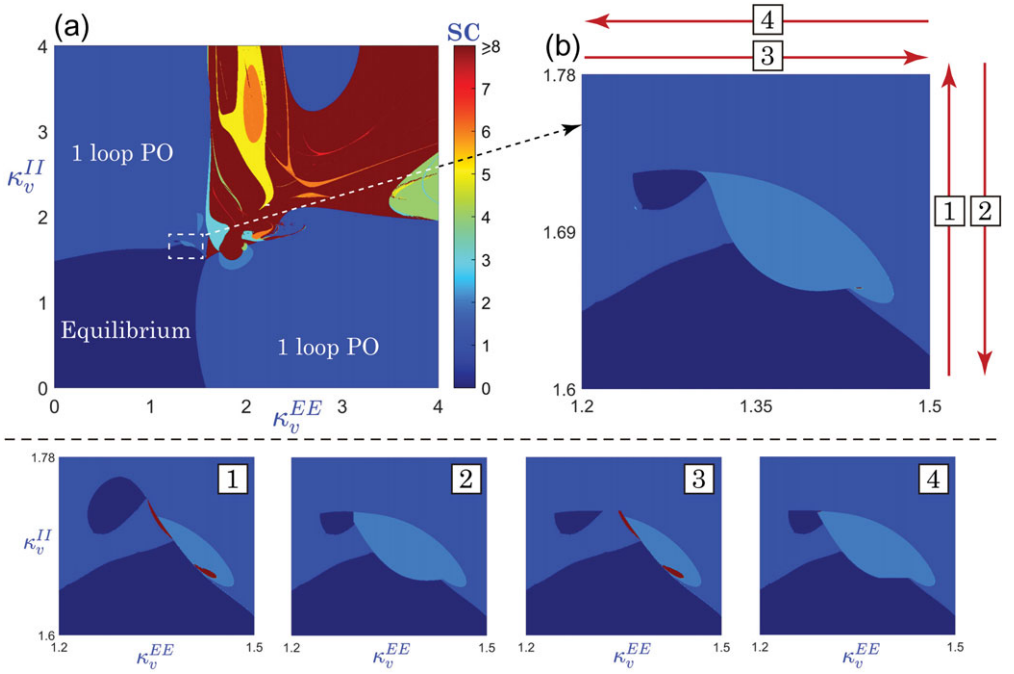

Figure 9. Parameter set P1. (a) Two-parameter spike-counting (SC) plot. (b) Magnification around the central part of plot (a). Plots 1–4 are obtained using different sets of initial conditions (more details in the text) showing different multistabilities.

attractors. This suggests that a plethora of bifurcations of codimension one and two are expected to be present in this region as we will show later.

A similar plot to figure 5 is shown in figure 10 for the parameter set P1, showing the first LEs. In plot (a), we present again the spike-counting plot of panel (a) of figure 9 to illustrate the same horizontal (H) and vertical (V) cross sections as in figure 5. In plot (H1) we present the first three LEs. This picture shows that there are intervals with positive LEs, indicating chaotic attractors and two simultaneously positive indicating hyperchaos. Plot (H1a) shows a magnification on the hyperchaotic interval. Plot (H2) presents a bifurcation diagram showing windows of both periodic orbits and chaotic attractors. In plot (V1), we present the first three LEs. There are intervals with chaotic attractors, but also torus attractors as shown in the magnification (V1a). Plot (V2) presents a bifurcation diagram. Note that although there are differences with figure 5 all the main ingredients are present.

In figure 11, we present a plot of the equilibrium structure and bifurcations of the model, showing the number of homogeneous fixed points in the parameter plane. The colours of each region denote the different number of equilibria and the labels of the form *m*U*n*S indicate a region with m unstable and n stable equilibria, respectively. Owing to the high dimension of the system and its complexity, there are up to eight equilibria in the studied plane, but at most one is stable. Plot (a1) presents a magnification around the central part of plot (a) where a complex structure is detected. Numerous changes in the number of equilibria and in their stability indicate the presence of different bifurcations such as Hopf and saddle–node bifurcations that are studied in detail in plot (b). As in figure 6, plots (b) and (b1) present some bifurcation lines (of codimension one) and points (of codimension two) over a greyscale version of plots (a) and (a1), respectively. Again, the bifurcations define quite well some of the regions detected with the equilibria analysis. It is important to remark that the existence of several Hopf–Hopf bifurcations lead to the existence of secondary torus or NS bifurcations that give rise to the creation of, among others, a 2-torus orbit as described above in figure 10.

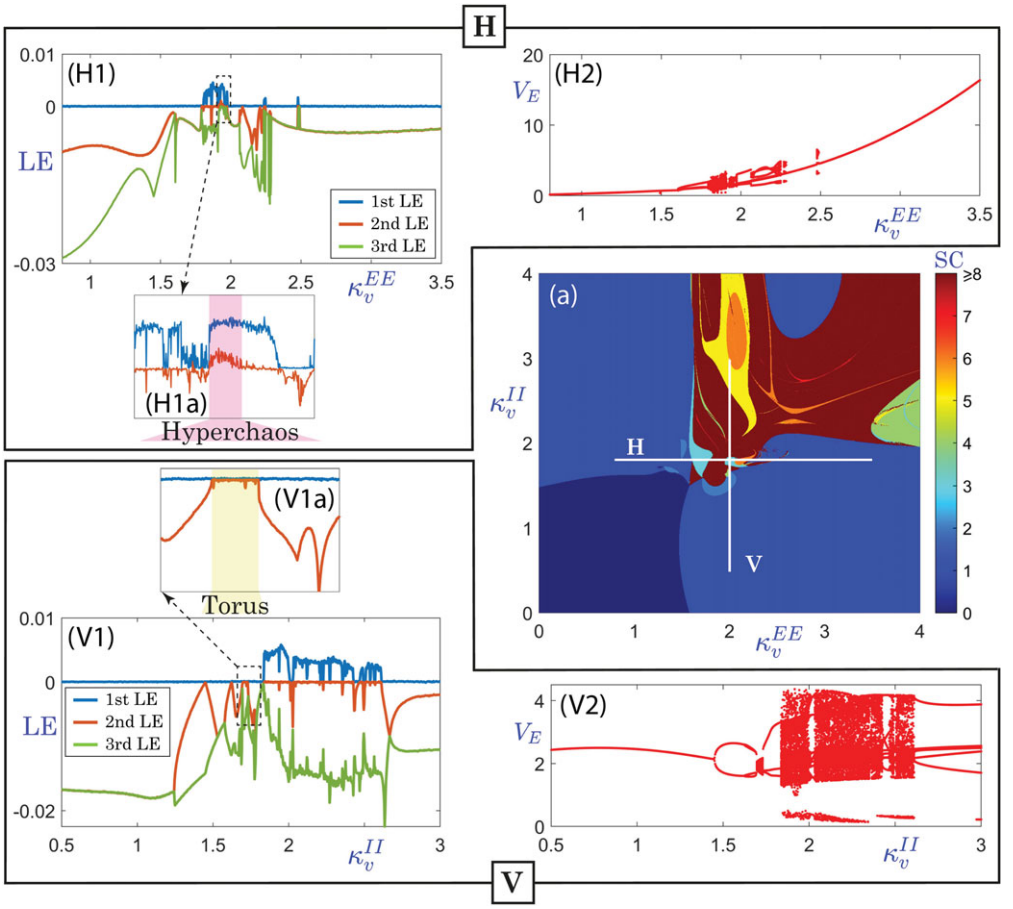

Figure 10. Parameter set P1. (a) Spike-counting (SC) bi-parametric sweep from figure 9. (H1) and (H1a), and (H2) shows the first LEs, and the bifurcation diagram, respectively, on the horizontal line fixing the parameter κ_v^{II} to 1.8 and the parameter κ_v^{EE} takes values in [0.8, 3.5]. (V1) and (V1a), and (V2) shows the first LEs, and the bifurcation diagram, respectively, on the vertical line fixing the parameter κ_v^{EE} to 2 and the parameter κ_v^{II} takes values in [0.5, 3.0].

In figure 12, we show different dynamics, from several stable periodic orbits (b) (clonic)–(c) (tonic) to emergent torus solutions (d) and chaotic dynamics (e) and (f) in between. The plot (a) presents the bi-parametric spike-counting plot with a circular parametric route on it. As we traverse this route, we cross from tonic to clonic dynamics through torus and chaotic dynamics as in figure 7. In the plots (b)–(f), we show a three-dimensional plot of the orbit in the (V_E, R_E, V_I) variables to illustrate the different kind of dynamics and the time series of the $|Z_E|$ and V_E variables. All of these orbits can be connected by small changes in the parameter space, which means that several changes in the conditions of the system may allow the transitions among all these different dynamics. The equations of the circular parametric path we have followed are given by $\kappa_v^{EE} = 1.6 + 0.4\cos(\gamma - 5\pi/8)$, $\kappa_v^{II} = 2.0 + 0.75\sin(\gamma - 5\pi/8)$, $\gamma \in [0, 7\pi/4]$. The initial conditions are set to 0 in all orbits and the values for the parameters $(\kappa_v^{EE}, \kappa_v^{II})$ used to compute the orbits of panels (b)–(f) are (1.2304, 1.7130), (1.5195, 1.2654), (1.9578, 1.6647), (1.9889, 2.1757) and (1.6536, 2.7432), respectively.

As in figure 8, figure 13 also shows that a tonic–clonic seizure transition can be found organized around a central Hopf–Hopf bifurcation on the parameter set P1. The system first transitions into the tonic seizure state via a Hopf bifurcation giving rise to oscillations at a high single frequency. The system then crosses a secondary bifurcation and moves into the transition region. The single frequency gives way to more complex behaviour, including regions of quasi-periodicity and

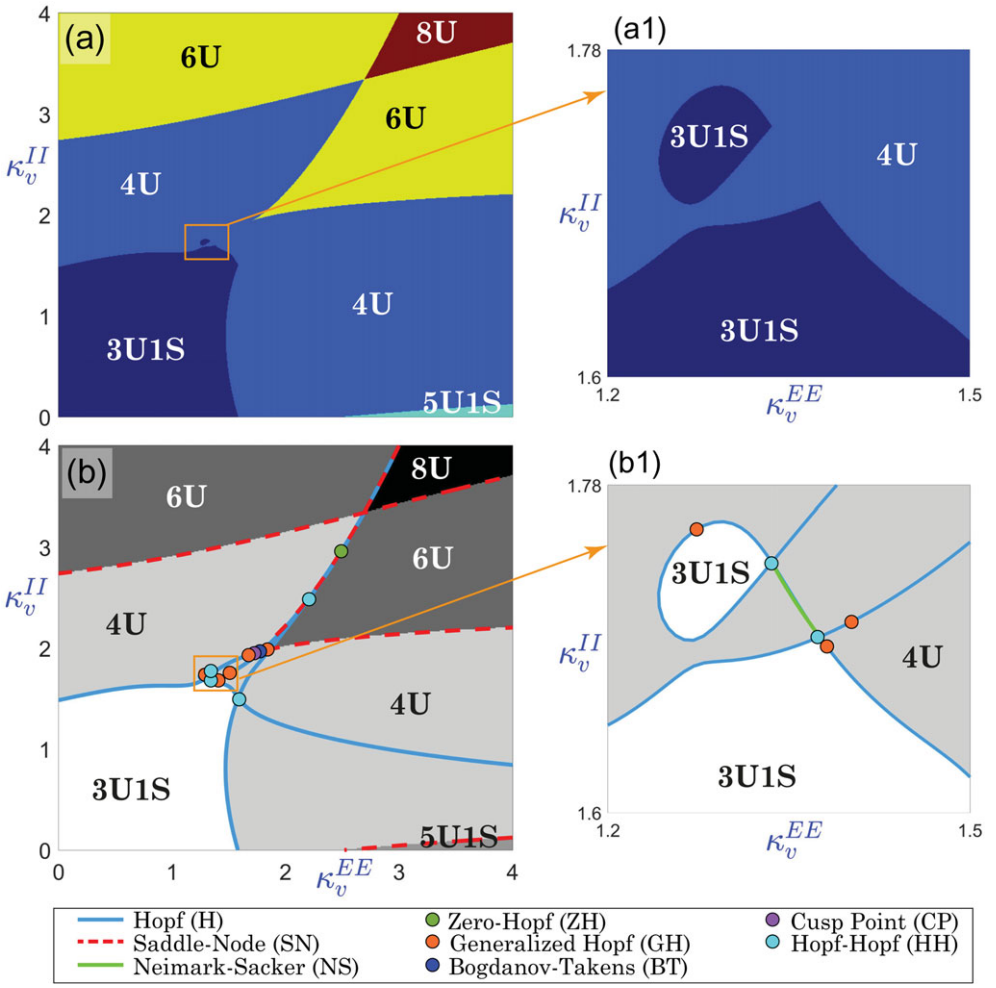

Figure 11. Parameter set P1. (a) Plot showing the number of homogeneous fixed points in the parameter plane $(\kappa_v^{EE}, \kappa_v^{II})$. (a1) Magnification around the centre part of plot (a). (b) and (b1) Primary bifurcations of equilibria, and several codimension-two points, as well as secondary torus or NS bifurcations, superimposed over a greyscale version of (a) and (a1), respectively.

chaos. As the system approaches the bifurcation boundary the new frequency becomes dominant until a simple limit cycle is restored on crossing the bifurcation boundary. The seizure may then progress back beyond the Hopf bifurcation corresponding to the seizure termination or may remain in this final state. Figure 13 demonstrates in the parameter set P1 an example trajectory in which the model parameters slowly vary along an arc in the $(\kappa_v^{EE}, \kappa_v^{II})$ plane (shown in figure 12) traversing around the organizing region identified by the numerical bifurcation analysis.

5. Spatio-temporal patterning

Epilepsy is a disorder of abnormal spatio-temporal organization in the brain. Mathematical models that incorporate spatial structure can potentially explain where seizures start, how they spread, what patterns they form and how they can be controlled, making them far more powerful and clinically relevant than non-spatial models. The analysis in §4 emphasizes the very rich temporal dynamics of the next-generation neural field model albeit for spatially homogenous solutions described by a system of ODEs. Thus, it does not give any insight into the stability of these states in the full integro-differential model or the spatial patterns that may be observed. Of course, the Turing analysis of §3 can be used to shed light on this, although is restricted to

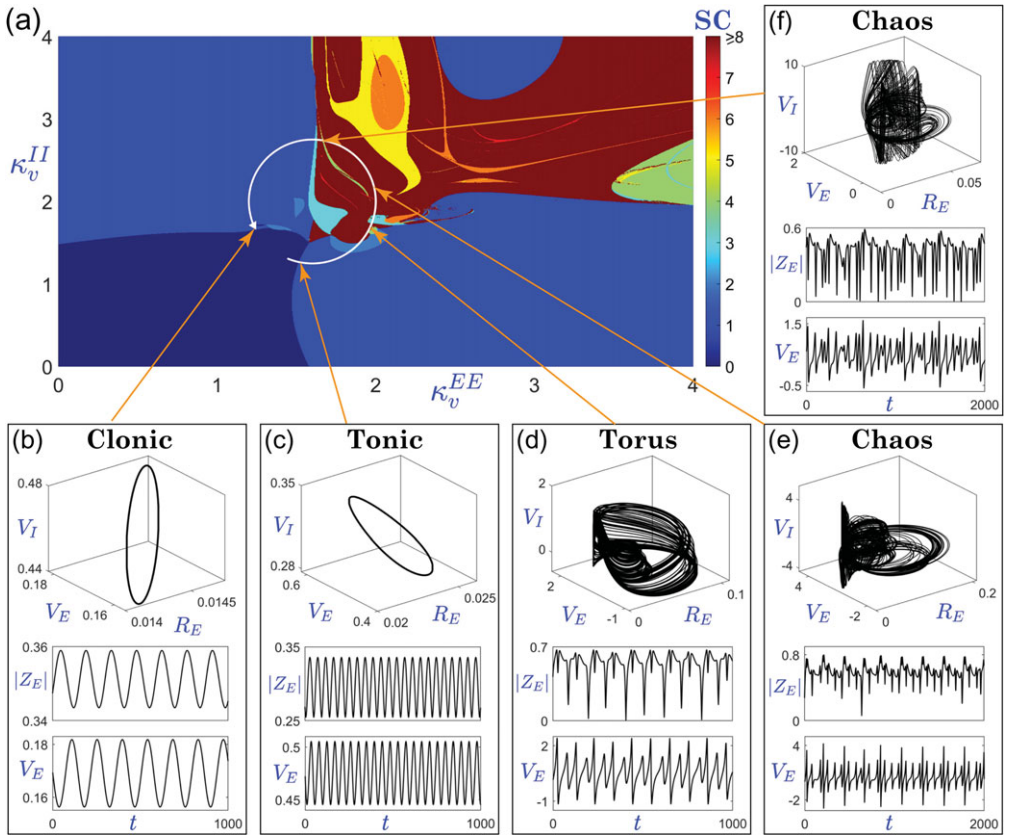

Figure 12. Parameter set P1. Plots of emergent torus solutions at points across the parameter space of figure 9. (a) Bi-parametric spike-counting plot with a circular path from tonic to clonic patterns. (b) and (c) Tonic and clonic periodic orbits. (d) Invariant torus. (e) and (f) Chaotic attractors.

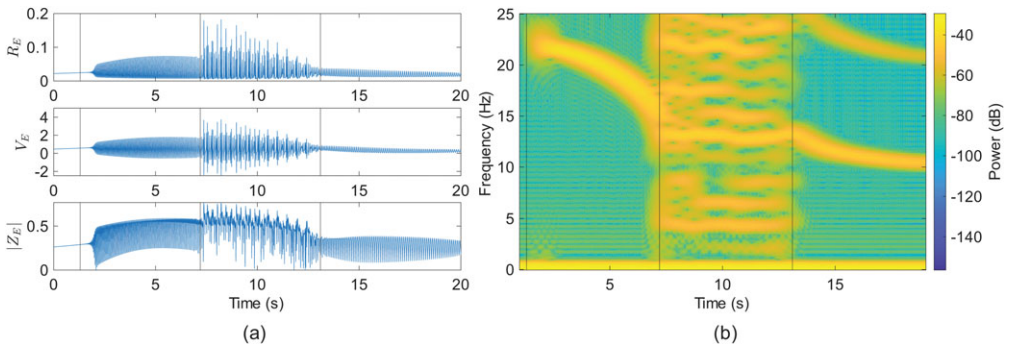

Figure 13. Parameter set P1. Dynamics of the space-clamped model following a slowly varying path travelling anticlockwise through parameter space as shown as a white curve in figure 12. The path passes around the complex of bifurcation points containing the Hopf–Hopf bifurcation. (a) Time series in R_E, V_E and $|Z_E|$ of the space-clamped model. (b) The corresponding spectrogram generated using a short-time Fourier transform of the generated time series for R_E in the space-clamped model, with black lines to indicate crossing of bifurcations. The dynamics are qualitatively similar to the case with parameter set P2 shown in figure 8.

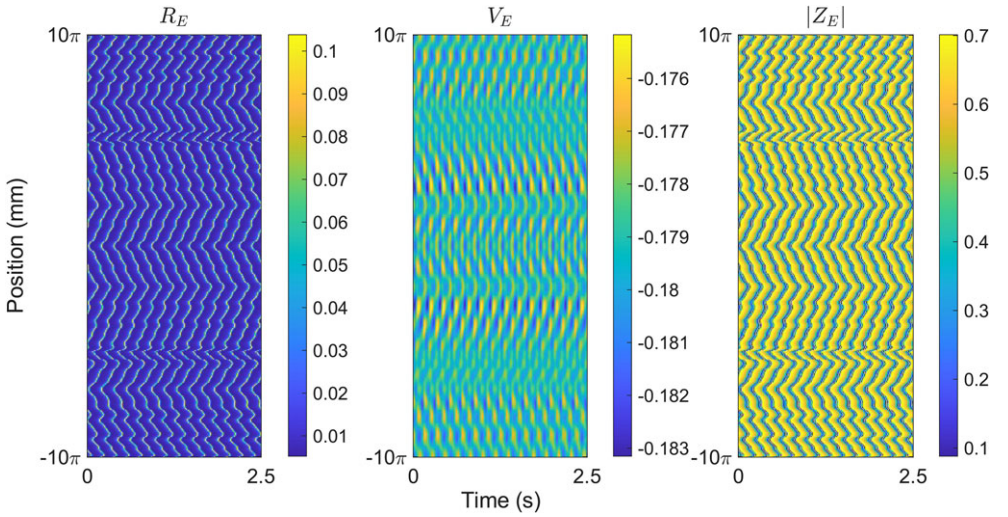

Figure 14. Space–time plots of the full next-generation neural field model in one spatial dimension. Parameters are chosen so that the space-clamped model exhibits quasi-periodic temporal solutions ($\kappa_v^{EE} = 2$, $\kappa_v^{II} = 1.325$). Each panel shows the mean firing rate, membrane potential and synchrony, respectively, for the excitatory population.

the neighbourhood of an instability of a spatially uniform state. In this case, we would recover the steady-state instability results of the space-clamped system with the restriction to *bulk modes* with $k = 0$. However, it is important to not overly rely on the analysis of space-clamped solutions as states such as those in figure 12 can be stable in the space-clamped system and unstable in the full system. To explore the excitation of non-bulk modes, including travelling waves, and the behaviour of such solutions as one moves more into the nonlinear regime, it is natural to make use of numerical simulations. In this section, we pursue this to complement the tonic–clonic story developed above with a study of associated spatial patterning.

The challenge of numerically solving the full integro-differential equation model is somewhat reduced with a judicious and natural choice of exponentially decaying connectivity function equation (2.6). This gives rise to a PDE model in the spirit of the Nunez brain wave equation that can be approximated using a finite-difference scheme [23]. In particular, this makes it numerically easier to handle the space-dependent axonal delays; see appendices A and C for further details. However, other more general numerical approaches for simulating neural field models with space-dependent delays are also available [37].

The space-clamped model suggests a plethora of interesting temporal dynamics in the transition region beyond the Hopf–Hopf bifurcation. The addition of the spatial dynamics can increase the complexity in this region and lead to some variation in the precise location of the points of instability as seen in §3. However, the predictions made do yield insight into the full model. We simulate the full model for a choice of parameters in this region and demonstrate the existence of the predicted quasi-periodic temporal dynamics: an example simulation in one spatial dimension is shown in figure 14 exhibiting the spatio-temporal dynamics giving rise to quasi-periodic behaviour. The equivalent dynamics in the two-dimensional planar model is given in the electronic supplementary material as a video (**S1**), and the pattern is shown at a fixed instant of time for R_E, V_E and $|Z_E|$ in figure 15. The model gives rise to a periodic grid pattern. In two dimensions, there is a wider range of available spatial instabilities, in this case the homogenous steady state is weakly perturbed by a spatially periodic mode with wavenumber motivated from the stability analysis and additive noise. For these parameters, we observe a temporally periodic square grid pattern. These simulations in both one and two spatial domains demonstrate the emergence of complex temporal rhythms as predicted by the space-clamped model.

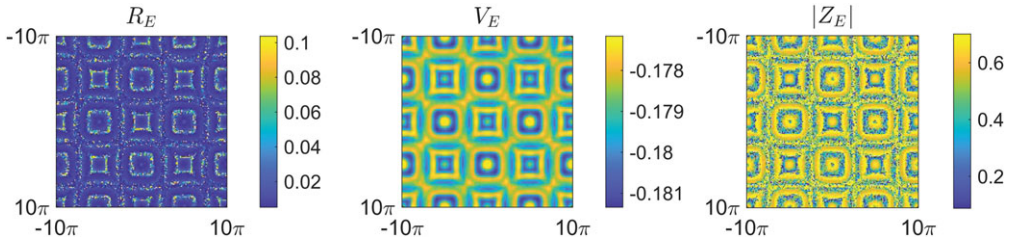

Figure 15. Snapshots at time $t = 2.375$ s of R_E, V_E and $|Z_E|$ showing the spatio-temporal pattern seen in the full neural field model simulated in two spatial dimensions. The model gives rise to a periodic grid pattern. A video of the temporal dynamics is shown in the electronic supplementary material (**S1**).

In many seizures, there is clear evidence of travelling wave dynamics. For example, in focal seizures, the seizure begins in a specific brain region known as the seizure focus. This focus then stimulates travelling waves which travel across the brain [38]. While tonic–clonic seizures can appear initially generalized, it is also possible for one to be initialized for a seizure focus in what are known as focal to bilateral tonic–clonic seizures.

To illustrate the generalization of seizure activity within the full spatio-temporal model, we pose the system at a seizure boundary (bifurcation) in the model parameter space. We then provide an initial localized perturbation in the form of a depolarization to a small region. Figure 16 shows the propagation of an initial bump of activity into a fully generalized oscillatory seizure-like state in one spatial dimension and figure 17 shows a snapshot of the complex radial spatio-temporal pattern that can form for this case in two spatial dimensions. A video of the full spatio-temporal dynamics for this case in two dimensions can be seen in the electronic supplementary material (**S2**). In both cases we can see the propagation of a front starting from the central depolarization and giving rise to periodic travelling waves behind the front. For one spatial dimension the effect of the finite domain used for simulation becomes apparent. As the front propagates and occupies an increasing proportion of the domain there is a critical point at which the whole domain is recruited into the oscillations leading to global, bulk oscillations outside the front. This behaviour is not observed in the model posed on a very large finite domain but is expected in bounded models of the brain, where localized (focal) seizure activity can propagate and generalize into generalized oscillations across the cortex.

6. Conclusion

In this paper, we have shown that a recently developed next-generation neural field model has the prerequisite biological features necessary to generate spontaneous dynamical behaviour reminiscent of that seen in tonic–clonic seizures. As well as a distinction between excitatory and inhibitory neuronal sub-populations (a feature of many earlier neural field models of the Wilson–Cowan type), the model incorporates a more realistic description of population activity that tracks both population rate and average voltage. This is in contrast to the common phenomenological approach of closing the equations of neural motion with a simple transduction of activity by a sigmoidal firing rate function. Nonetheless, it is fair to recognize that such traditional approaches have had some success in explaining seizure dynamics with the inclusion of a second inhibitory population [39]. Importantly, the biological realism of the model presented here (it being derived from an underlying spiking neural system) means that it is natural and straightforward to incorporate other important components of cortical processing, such as arising from chemical synapses and axonal delays. Building on the observation that electrical synapses (often ignored in standard neural field models) can have a significant role to play in coordinating large-scale cortical dynamics [16], we have paid careful attention to their ability to organize bifurcations that are central to understanding tonic–clonic seizure transitions. Indeed, electrical synapses mediated

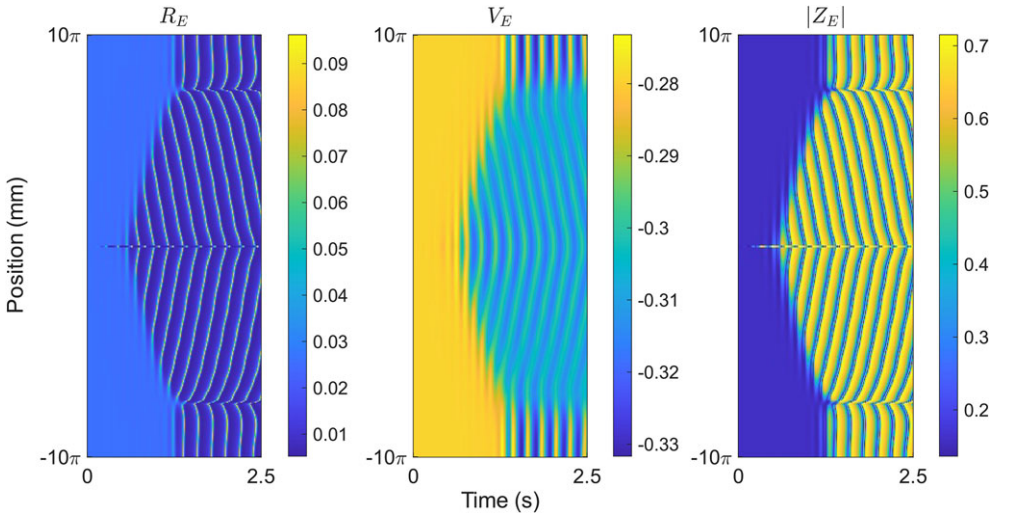

Figure 16. Space–time plot of the full spatio-temporal model (in one spatial dimension) following a localized perturbation to the steady state by depolarizing the excitatory neuronal populations in a small region in the centre of the domain. The local perturbation propagates outward leading to the oscillations spreading across the cortical surface and the generalization of the seizure-like state from a single focus. Each panel shows the mean firing rate, membrane potential and synchrony, respectively, for the excitatory population.

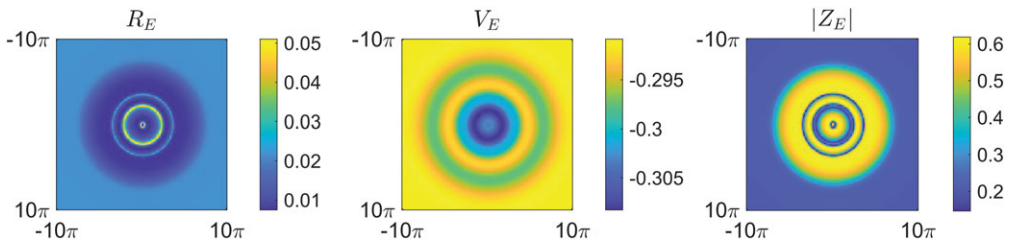

Figure 17. Snapshots at time $t = 2.375$ s of R_E, V_E, $|Z_E|$ showing the spatio-temporal pattern seen in the full neural field model simulated in two spatial dimensions following a localized perturbation to the excitatory population centred on (0, 0). The perturbation grows radially forming a periodic oscillating pattern of concentric circles. A video of the temporal dynamics for $|Z_E|$ is shown in the electronic supplementary material (**S2**).

by gap junctions have long been known to play an important role in the generation of pathological brain rhythms [7]. We have identified Hopf–Hopf bifurcations, in which two branches of Hopf bifurcations producing oscillations with different and incommensurate frequencies intersect, as a key organizing centre. Importantly, we have shown that the next-generation neural field model with gap junctions can robustly generate these as well as a host of secondary torus bifurcations. These results have been obtained with a mixture of numerical bifurcation analysis of the space-clamped model (highlighting a rich and complex bifurcation structure) and a Turing analysis (for determining useful spectral properties) of the full spatio-temporal model. This provides a mechanism to achieve quasi-periodicity through the creation of two limit cycles by crossing two branches of Hopf bifurcations, one stable and one unstable. Two branches of torus bifurcations appear generically from Hopf–Hopf bifurcations and on crossing destabilize the stable branch of periodic orbits. The bifurcation analysis has been done for two sets of parameters in order to show the robustness of the proposed hypothesis. Guided by the bifurcation structure of the space-clamped model, we have been able to choose plausible paths through parameter space

and observe a connecting branch of quasi-periodic solutions in the full spatio-temporal model as it transitions between two incommensurate frequencies. As well as the tonic–clonic transition, numerical studies (in one- and two-dimensional spatial domains) have been used to illustrate some of the other rich and complex behaviours that are present in the model as well as its ability to generate chaotic dynamics.

For achieving a tonic–clonic seizure transition within the model, we have focused on paths that describe changes in the strength of gap junction coupling since a slow modulation of electrical synapses is known to occur during seizures [36,40]. In more detail, this arises because of interaction with the local extracellular potassium concentration [41]. In future work, it will be interesting to augment the neural field presented here and couple it to a (reaction–diffusion) model for extracellular potassium combined with rules for the closing of gap junctions caused by the slow acidification of the extracellular environment that occurs during seizures. Moreover, it is important to remember that many forms of seizure involve the thalamus and one should be mindful of an overly cortical perspective [42]. In much the same way that traditional neural mass and field models can be extended to include a thalamic component, e.g. [43], the next-generation model presented here can be coupled to firing rate models of thalamo–cortical relay and reticular cells expressing slow rebound currents [44]. This is relevant for further uncovering candidate biophysical mechanisms for the propagation, onset and termination of seizures and is a topic of current investigation.

Data accessibility. The data are provided in the electronic supplementary material [45].

Declaration of AI use. We have not used AI-assisted technologies in creating this article.

Authors' contributions. O.C.: formal analysis, investigation, writing—original draft and writing—review and editing; A.M-C.: formal analysis, investigation, writing—original draft and writing—review and editing; R.D.O'D.: formal analysis, investigation, supervision, writing—original draft, writing—review and editing; R.B.: formal analysis, investigation, supervision, writing—original draft, writing—review and editing; S.C.: conceptualization, formal analysis, project administration, writing—original draft, writing—review and editing.

All authors gave final approval for publication and agreed to be held accountable for the work performed therein.

Conflict of interest declaration. We declare we have no competing interests.

Funding. This work was supported by the Medical Research Council (grant no. MR/N013913/1). R.B. and A.M.-C. have been supported by the Spanish Research project PID2021-122961NB-I00 and PID2024-156032NB-I00 and by the European Regional Development Fund and Diputación General de Aragón E24-23R. R.B. has been supported by the Spanish Research project TED2021-130459B-I00 and by the European Regional Development Fund and Diputación General de Aragón (E24-20R and LMP94-21).

Appendix A. Brain wave equation

For a recent discussion of the derivation of the brain wave equation from a non-local and delayed source term in a neural field, see [46, ch. 9]. In one spatial dimension, the choice equation (2.6) gives the equivalent PDE for $\psi_{ab}(x,t)$ as

$$\left[\left(\frac{1}{\sigma_{ab}}+\frac{1}{v_{ab}}\frac{\partial}{\partial t}\right)^2-\frac{\partial 2}{\partial x}\right]\psi_{ab}=\frac{1}{\sigma_{ab}}\left(\frac{1}{\sigma_{ab}}+\frac{1}{v_{ab}}\frac{\partial}{\partial t}\right)R_b. \tag{A 1}$$

In two spatial dimensions, the choice equation (3.15) yields the *approximate* PDE for $\psi_{ab}(\boldsymbol{r},t)$,

$$\left[\left(\frac{1}{\sigma_{ab}}+\frac{1}{v_{ab}}\frac{\partial}{\partial t}\right)^2-\frac{3}{2}\nabla^2\right]\psi_{ab}=\sigma_{ab}^{-2}R_b. \tag{A 2}$$

This PDE is approximate in the sense that it is only expected to accurately capture the behaviour of long wavelength patterns. However, it can be viewed as an exact description for the choice $w(\boldsymbol{r})=K_0(\sqrt{2/3}|\boldsymbol{r}|/\sigma_{ab})/(3\pi\sigma_{ab}^2)$, where K_0 is the modified Bessel function of the second kind of order zero. When considering space-clamped solutions of a brain wave equation, we simply set spatial derivatives to zero and replace $\partial/\partial t$ by $\mathrm{d}/\mathrm{d}t$ to obtain a system of ODEs.

Table 1. Parameter set P1 yielding tonic oscillations with a frequency of approximately 10 Hz and slower clonic oscillations with a frequency of approximately 6 Hz.

parameter	value	parameter	value	parameter	value	parameter	value
η_E	0.343	η_I	0.026	κ_v^{EI}	0	κ_v^{IE}	0
κ_v^{II}	$\in [0, 4]$	κ_v^{EE}	$\in [0, 4]$	κ_s^{EE}	3.5	κ_s^{EI}	4
κ_s^{IE}	3	κ_s^{II}	2	τ_E	11	τ_I	12
α_{EE}	0.1	α_{EI}	0.05	α_{IE}	0.1	α_{II}	0.05
Δ_E	0.5	Δ_I	0.5	v_{syn}^{EE}	10	v_{syn}^{EI}	−10
v_{syn}^{IE}	10	v_{syn}^{II}	−10	v	12	σ_{EE}	10
σ_{EI}	2	σ_{IE}	10	σ_{II}	2		

Table 2. Parameter set P2 yielding tonic oscillations with a frequency of approximately 10 Hz and slower clonic oscillations with a frequency of approximately 6 Hz.

parameter	value	parameter	value	parameter	value	parameter	value
η_E	0.2	η_I	0.15	κ_v^{EI}	0	κ_v^{IE}	0
κ_v^{II}	$\in [0, 4]$	κ_v^{EE}	$\in [0, 4]$	κ_s^{EE}	3.5	κ_s^{EI}	4
κ_s^{IE}	2	κ_s^{II}	2	τ_E	11	τ_I	12
α_{EE}	0.1	α_{EI}	0.05	α_{IE}	0.1	α_{II}	0.05
Δ_E	0.5	Δ_I	0.5	v_{syn}^{EE}	10	v_{syn}^{EI}	−10
v_{syn}^{IE}	10	v_{syn}^{II}	−10	v	12	σ_{EE}	20
σ_{EI}	100	σ_{IE}	20	σ_{II}	100		

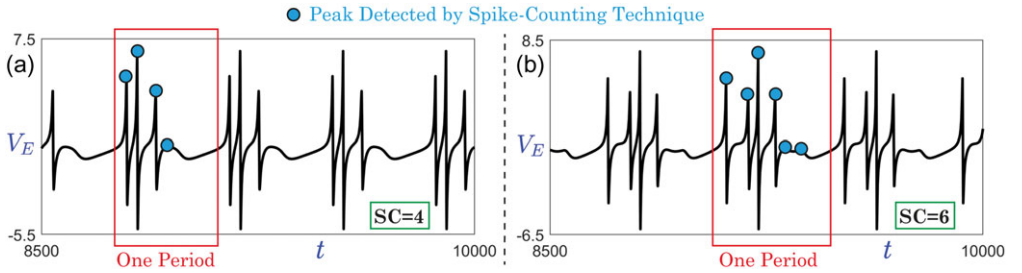

Figure 18. (a) and (b) Time series of two periodic orbits with 4 and 6 peaks, respectively. The blue dots correspond to the detections of the spike-counting (SC) technique (in this case detecting the local maxima). The initial conditions for both orbits are 0 for all the variables and the values for the parameters (κ_v^{EE}, κ_v^{II}) are (2.5, 1.9) for panel (a) and (2.5, 3.5) for panel (b), and with other parameters taken from parameter set P2.

Appendix B. Standard parameter sets

The values of the parameter set P1 are listed in table 1 and those for P2 in table 2. All time units are in milliseconds and lengths are in millimetres.

Appendix C. Numerical methodologies and code

The spike-counting technique that we employ consists of selecting a Poincaré section or imposing

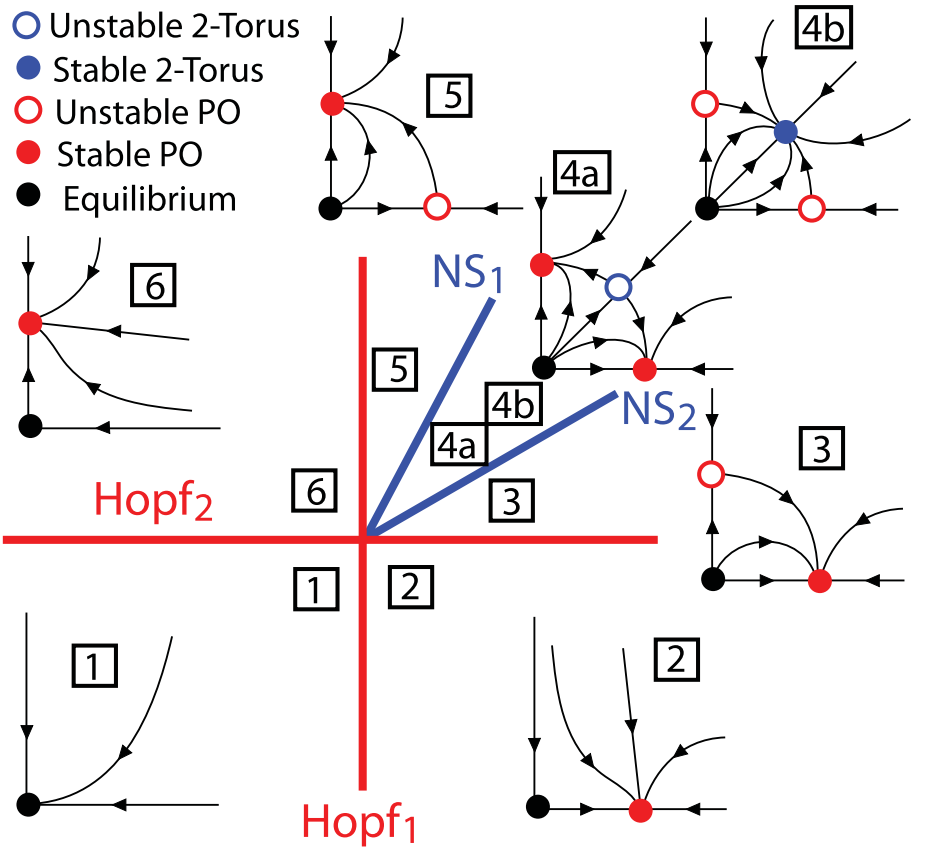

Figure 19. Unfolding of two standard cases of Hopf–Hopf bifurcation in polar coordinates r_1 and r_2.

a condition such as detecting the relative maxima of an orbit (which is the condition used in this article) [32]. After a long transient integration (to access the periodic, toroidal or chaotic asymptotic state), we determine the points of relative maxima (and the period if the trajectory converges to a periodic orbit). In figure 18, we present as an example the detected points (local maxima) for two periodic orbits. The algorithm stops when a new point (maximum) is equal, up to a fixed tolerance, to a previously calculated maximum (i.e. we calculate the period when the orbit is periodic). In order to distinguish between qualitatively different trajectories, a colour is assigned to each number of maxima per cycle length. To obtain the spike-counting plots, we integrate from 0 to 30 000 as transient time and then integrate again from 0 to 6000 using the advanced capabilities of the Taylor series numerical integrator TIDES [47][1] that allows a continuous output, very suitable for the location of the maxima of trajectories.

A Runge–Kutta integrator of order five (with time step 0.001) is used to obtain the time series for use with the algorithm in [33] for computing (an approximation of) the LEs. In these numerical calculations, a transient time from 0 to 10 000 is used to generate initial conditions for subsequent integration from 0 to 50 000. The initial conditions in all the plots are set to 0 for all the variables and the identity matrix for the variational equations.

The computation of the bifurcation curves is done using the free software MATCONT [31].

The simulations of full spatio-temporal dynamics are performed by using a second-order central difference to discretize the spatial domain. The infinite domain is approximated by using a

[1]See https://sourceforge.net/projects/tidesodes/.

large domain with periodic boundary conditions. The resulting ODE system is then solved using DifferentialEquations.jl [48] with an order five Runge–Kutta scheme [49].

Appendix D. Hopf–Hopf bifurcation

In polar coordinates, the normal form of the Hopf–Hopf bifurcation is given by [50,51]

$$\left.\begin{aligned}\dot{r}_1 &= r_1(\mu_1 + p_{11}r_1^2 + p_{12}r_2^2 + s_1 r_2^4),\\ \dot{r}_2 &= r_2(\mu_2 + p_{21}r_1^2 + p_{22}r_2^2 + s_2 r_1^4),\\ \dot{\phi}_1 &= \omega_1\\ \text{and}\qquad \dot{\phi}_2 &= \omega_2,\end{aligned}\right\}$$

where μ_1 and μ_2 are the bifurcation parameters. The signs of the coefficients p_{ij} determine the kind of Hopf–Hopf bifurcation. In this paper, we do not attempt to detail all the cases and possible situations, and instead focus on the generic situation. In figure 19, we present the theoretical unfolding of two standard cases of Hopf–Hopf bifurcation. That is, the situation where at the Hopf–Hopf bifurcation a pair of torus or NS bifurcations appear developing a stable (case –4a– in the figure) or unstable torus (case –4b–). In the figure, the equilibria of the (r_1, r_2) subsystem (red circles) on the axes are limit cycles (PO) of the full system and those off-axis (blue circles) represent a 2-torus.

References

1. World Health Organization. 2019 Epilepsy: a public health imperative. Technical documents World Health Organization Geneva.
2. Stafstrom C, Carmant L. 2015 Seizures and epilepsy: an overview for neuroscientists. *Cold Spring Harbor Perspect. Med.* **5**, a022426. (doi:10.1101/cshperspect.a022426)
3. Sarmast ST, Abdullahi AM, Jahan N. 2020 Current classification of seizures and epilepsies: scope, limitations and recommendations for future action. *Curēus (Palo Alto, CA)* **12**, e10549–e10549. (doi:10.7759/cureus.10549)
4. Ermentrout GB, Cowan JD. 1980 Secondary bifurcation in neuronal nets. *SIAM J. Appl. Math.* **39**, 323–340. (doi:10.1137/0139028)
5. Cook BJ, Peterson ADH, Woldman W, Terry JR. 2022 Neural field models: a mathematical overview and unifying framework. *Math. Neurosci. Appl.* **2**, 1–67. (doi:10.46298/mna.7284)
6. Visser S, Nicks R, Faugeras O, Coombes S. 2017 Standing and travelling waves in a spherical brain model: the Nunez model revisited. *Physica D* **349**, 27–45. (doi:10.1016/j.physd.2017.02.017)
7. Velazquez JLP, Carlen PL. 2000 Gap junctions, synchrony and seizures. *Trends Neurosci.* **23**, 68–74. (doi:10.1016/S0166-2236(99)01497-6)
8. Modhara S, Lai YM, Thul R, Coombes S. 2021 Neural fields with rebound currents: Novel routes to patterning. *SIAM J. Appl. Dyn. Syst.* **20**, 1596–1620. (doi:10.1137/20M1364710)
9. Luke TB, Barreto E, So P. 2013 Complete classification of the macroscopic behavior of a heterogeneous network of theta neurons. *Neural Comput.* **25**, 3207–3234. (doi:10.1162/NECO_a_00525)
10. Montbrió E, Pazó D, Roxin A. 2015 Macroscopic description for networks of spiking neurons. *Phys. Rev. X* **5**, 021028. (doi:10.1103/PhysRevX.5.021028)
11. Byrne A, O'Dea RD, Forrester M, Ross J, Coombes S. 2020 Next-generation neural mass and field modeling. *J. Neurophysiol.* **123**, 726–742. (doi:10.1152/jn.00406.2019)
12. Coombes S. 2023 Next generation neural population models. *Front. Appl. Math. Stat.* **9**, 1128224. (doi:10.3389/fams.2023.1128224)
13. Byrne A, Brookes MJ, Coombes S. 2017 A mean field model for movement induced changes in the beta rhythm. *J. Comput. Neurosci.* **43**, 143–158. (doi:10.1007/s10827-017-0655-7)
14. Byrne A, Ross J, Nicks R, Coombes S. 2022 Mean-field models for EEG/MEG: from oscillations to waves. *Brain Topogr.* **35**, 36–53. (doi:10.1007/s10548-021-00842-4)
15. Rabuffo G, Fousek J, Bernard C, Jirsa V. 2021 Neuronal cascades shape whole-brain functional dynamics at rest. *eNeuro* **8**, ENEURO.0283-21.2021. (doi:10.1523/ENEURO.0283-21.2021)

16. Forrester M, Petros S, Cattell O, Lai YM, O'Dea RD, Sotiropoulos S, Coombes S. 2024 Whole brain functional connectivity: insights from next generation neural mass modelling incorporating electrical synapses. *PLoS Comput. Biol.* **20**, e1012647. (doi:10.1371/journal.pcbi.1012647)
17. Nunez PL. 1995 *Neocortical dynamics and human EEG rhythms*. Oxford: Oxford University Press.
18. Coombes S, Beim Graben PP, Potthast R, Wright J. 2014 *Neural fields: theory and applications*. Berlin, Germany: Springer.
19. Wilson HR, Cowan JD. 1972 Excitatory and inhibitory interactions in localized populations of model neurons. *Biophys. J.* **12**, 1–24. (doi:10.1016/S0006-3495(72)86068-5)
20. Wilson HR, Cowan JD. 1973 A mathematical theory of the functional dynamics of cortical and thalamic nervous tissue. *Kybernetik* **13**, 55–80. (doi:10.1007/BF00288786)
21. Revell AY *et al.* 2025 White matter signals reflect information transmission between brain regions during seizures. *Brain* **149**, 77–89. (doi:10.1093/brain/awaf444)
22. Wang XJ, Kennedy H. 2016 Brain structure and dynamics across scales: in search of rules. *Curr. Opin Neurobiol.* **37**, 92–98. (doi:10.1016/j.conb.2015.12.010)
23. Nunez PL. 1974 The brain wave equation: a model for the EEG. *Math. Biosci.* **21**, 279–297. (doi:10.1016/0025-5564(74)90020-0)
24. Crodelle J, Zhou D, Kovačič G, Cai D. 2019 A role for electrotonic coupling between cortical pyramidal cells. *Front. Comput. Neurosci.* **13**, 33. (doi:10.3389/fncom.2019.00033)
25. Crodelle J, Zhou D, Kovačič G, Cai D. 2020 A computational investigation of electrotonic coupling between pyramidal cells in the cortex. *J. Comput. Neurosci.* **48**, 1–21. (doi:10.1007/s10827-020-00762-5)
26. Galarreta M, Hestrin S. 1999 A network of fast-spiking cells in the neocortex connected by electrical synapses. *Nature* **402**, 72–75. (doi:10.1038/47029)
27. Gibson JR, Beierlein M, B W Connors BW. 1999 Two networks of electrically coupled inhibitory neurons in neocortex. *Nature* **402**, 75–79. (doi:10.1038/47035)
28. Connors BW, Long MA. 2004 Electrical synapses in the mammalian brain. *Annu. Rev. Neurosci.* **27**, 393–418. (doi:10.1146/annurev.neuro.26.041002.131128)
29. Mercer A, Bannister AP, Thomson AM. 2006 Electrical coupling between pyramidal cells in adult cortical regions. *Brain Cell Biol.* **35**, 13–27. (doi:10.1007/s11068-006-9005-9)
30. Wang Y, Barakat A, Zhou H. 2010 Electrotonic coupling between pyramidal neurons in the neocortex. *PLoS ONE* **5**, e10253. (doi:10.1371/journal.pone.0010253)
31. Dhooge A, Govaerts W, Kuznetsov YA, Meijer HGE, Sautois B. 2008 New features of the software MatCont for bifurcation analysis of dynamical systems. *Math. Comput. Modell. Dyn. Syst.* **14**, 147–175. (doi:10.1080/13873950701742754)
32. Barrio R, Shilnikov A. 2011 Parameter-sweeping techniques for temporal dynamics of neuronal systems: case study of Hindmarsh-Rose model. *J. Math. Neurosci.* **1**, 1–22. (doi:10.1186/2190-8567-1-6)
33. Wolf A, Swift JB, Swinney HL, Vastano JA. 1985 Determining Lyapunov exponents from a time series. *Physica D* **16**, 285–317. (doi:10.1016/0167-2789(85)90011-9)
34. Raimondo JV, Burman RJ, Katz AA, Akerman CJ. 2015 Ion dynamics during seizures. *Front. Cellular Neurosci.* **9**, 419. (doi:10.3389/fncel.2015.00419)
35. Srinivas M, Calderon DP, Kronengold J, Verselis VK. 2005 Regulation of connexin hemichannels by monovalent cations. *J. Gen. Physiol.* **127**, 67–75. (doi:10.1085/jgp.200509397)
36. Martinet LE, Fiddyment G, Madsen J, Eskandar E, Truccolo W, Eden U, Cash S, Kramer M. 2017 Human seizures couple across spatial scales through travelling wave dynamics. *Nat. Commun.* **8**, 14896–14896. (doi:10.1038/ncomms14896)
37. Hutt A, Rougier N. 2010 Activity spread and breathers induced by finite transmission speeds in two-dimensional neural fields. *Phys. Rev. E* **82**, 055701. (doi:10.1103/PhysRevE.82.055701)
38. Diamond JM, Diamond BE, Trotta MS, Dembny K, Inati SK, Zaghloul KA. 2021 Travelling waves reveal a dynamic seizure source in human focal epilepsy. *Brain* **144**, 1751–1763. (doi:10.1093/brain/awab089)
39. Fan D, Wang Q, Perc M. 2015 Disinhibition-induced transitions between absence and tonic-clonic epileptic seizures. *Sci. Rep.* **5**, 12618. (doi:10.1038/srep12618)
40. Schlafly ED, Marshall FA, Merricks EM, Eden UT, Cash SS, Schevon CA, Kramer MA. 2022 Multiple sources of fast traveling waves during human seizures: resolving a controversy. *J. Neurosci.* **42**, 6966–6982. (doi:10.1523/JNEUROSCI.0338-22.2022)

41. Kocsis JD, Malenka RC, Waxman SG. 1983 Effects of extracellular potassium concentration on the excitability of the parallel fibres of the rat cerebellum. *J. Physiol.* **334**, 225–244. (doi:10.1113/jphysiol.1983.sp014491)
42. Steriade M. 2003 *Neuronal substrates of sleep and epilepsy*. Cambridge: Cambridge University Press.
43. Taylor PN, Baier G, Cash SS, Wang Y. 2013 A model of stimulus induced epileptic spike-wave discharges. In *2013 IEEE Symposium on Computational Intelligence, Cognitive Algorithms, Mind, and Brain (CCMB)*, pp. 53–59.
44. Coombes S. 2003 Dynamics of synaptically coupled integrate-and-fire-or-burst neurons. *Phys. Rev. E* **67**, 041910. (doi:10.1103/PhysRevE.67.041910)
45. Cattell O, Mayora-Cebollero A, O'Dea RD, Barrio R, Coombes S. 2026 Understanding tonic-clonic seizure transitions as secondary bifurcations in a neural field model. Figshare. (doi:10.6084/m9.figshare.c.8459650)
46. Coombes S, Wedgwood KCA. 2023 *Neurodynamics: an applied mathematics perspective*, vol. 75. Texts in Applied Mathematics. Berlin, Germany: Springer.
47. Abad A, Barrio R, Blesa F, Rodriguez M. 2012 Algorithm 924: TIDES, a Taylor series integrator for differential equations. *ACM Trans. Math. Softw.e (TOMS)* **39**, 1–28. (doi:10.1145/2382585.2382590)
48. Rackauckas C, Nie Q. 2017 Differentialequations.jl—a performant and feature-rich ecosystem for solving differential equations in julia. *J. Open Res. Softw.* **5**, 15. (doi:10.5334/jors.151)
49. Tsitouras C. 2011 Runge–Kutta pairs of order 5 (4) satisfying only the first column simplifying assumption. *Comput. Math. Appl.* **62**, 770–775. (doi:10.1016/j.camwa.2011.06.002)
50. Kuznetsov Y. 2004 *Elements of applied bifurcation theory*. Berlin, Germany: Springer.
51. Revel G, Alonso DM, Moiola JL. 2008 A gallery of oscillations in a resonant electric circuit: Hopf-Hopf and fold-flip interactions. *Int. J. Bifurcation Chaos* **18**, 481–494. (doi:10.1142/S0218127408020409)